SINGLE CELL COMPENDIUM OF THE MUSCLE MICROENVIRONMENT IN PERIPHERAL ARTERY DISEASE REVEALS CAPILLARY ENDOTHELIAL HETEROGENEITY AND ACTIVATION OF RESIDENT MACROPHAGES

Short title: scRNAseq of human skeletal muscle in PAD

Guillermo Turiel[1], MS; Thibaut Desgeorges[1], PhD; Evi Masschelein[1], PhD; Manuela Birrer[2], MD; Jing Zhang[1], PhD; Stephan Engelberger[2], MD; Katrien De Bock[1], PhD.

Affiliations: (1) Laboratory of Exercise and Health, Department of Health Sciences and Technology, Swiss Federal Institute of Technology (ETH), Zurich (Schwerzenbach), Switzerland; (2) Vascular Center, Department for General, Visceral and Vascular Surgery, Kantonsspital Baden, Baden, Switzerland

Total word count: 14913

Corresponding author:

Katrien De Bock

Email: katrien-debock@ethz.ch

Laboratory of Exercise and Health

Institute of Movement Sciences (D-HEST)

ETH Zürich - Swiss Federal Institute of Technology

ETH Zürich, SLA C7

Schorenstrasse 16

CH-8603 Schwerzenbach

Switzerland

Tel. +41 44 655 7389

Abstract

Background: Peripheral artery disease (PAD) is caused by atherosclerosis and chronic narrowing of lower limb arteries leading to decreased muscle perfusion and oxygenation. Current guidelines for treating PAD include endovascular strategies or bypass surgery but long-term outcomes have been suboptimal. This is likely due to our limited understanding of the contribution of the microvasculature as well as other cell types, in particular macrophages, to PAD skeletal muscle pathophysiology. We used single cell sequencing to investigate cellular and transcriptional heterogeneity of the skeletal muscle microenvironment in PAD.

Methods: Samples from the medial head of the *gastrocnemius* muscle of individuals undergoing either lower limb aneurysm surgery (controls) or PAD bypass surgery (PAD) were collected. Samples were either frozen for histological evaluation (control: n=4; PAD: n=6) or were immediately processed for single cell RNA sequencing of mononuclear cells (control: n=4; PAD: n= 4). Bioinformatic tools were used to annotate cell types and their subpopulations, to study transcriptional changes and to analyze cellular interactions.

Results: We generated a dataset comprised of 106,566 high-quality, deep-sequenced cells that compose the muscle microenvironment. Focusing on endothelial cells (ECs) and macrophages, we confirmed the presence of ATF3/4^{+} ECs with angiogenic and immune regulatory capacities in human muscle and found that their transcriptional profile profoundly alters during PAD. Also, capillary ECs display features of endothelial to mesenchymal transition. Furthermore, we identified *LYVE1*^{hi}MHCII^{low} resident macrophages as the dominant macrophage population in human muscle, even under a chronic inflammatory condition such as PAD. During PAD, *LYVE1*^{hi}MHCII^{low} macrophages get activated and acquire a more pro-inflammatory profile. Finally, we map strong intercellular communication in the muscle microenvironment, which is significantly altered in PAD.

Conclusions: The dataset we present here provides a highly valuable resource for gaining deeper insights into the critical roles that cells in the muscle microenvironment may play in PAD skeletal muscle pathology. We propose that targeting the crosstalk between ECs and macrophages could provide novel insights for developing effective treatments against this disease.

Keywords

1. Peripheral artery disease, human, skeletal muscle, endothelial cells, macrophages, single cell RNA sequencing

Nonstandard Abbreviations and Acronyms

PAD, peripheral artery disease; IC, intermittent claudication; CLI, critical limb ischemia; ABI, ankle brachial index; scRNAseq, single cell RNA sequencing; EC, endothelial cell; MoMac; monocytes/macrophages.

37 ## Introduction

38 Peripheral artery disease (PAD) is a common disorder caused by atherosclerosis and chronic
39 narrowing of lower limb arteries leading to decreased muscle perfusion and oxygenation. Worldwide,
40 more than 200 million people are diagnosed with PAD and numbers are still rising[1–3]. PAD patients
41 suffer from pain, fatigue, and discomfort in the limb muscles due to exercise-induced ischemia which
42 resolves after a short period of rest, a syndrome termed intermittent claudication (IC)[4,5]. Moreover, if
43 left untreated, persistent lack of lower limb perfusion can lead to critical limb ischemia (CLI), which
44 comprises rest pain, tissue loss and necrosis, ulcerations, and gangrene. In fact, PAD is the most
45 common cause of lower limb amputations in the western world[1]. The ultimate goal of PAD treatment
46 is to restore perfusion of the ischemic limb. Current guidelines for treating PAD mostly target large
47 atherosclerotic lesions in the feeding arteries of the lower limb and include endovascular strategies or
48 bypass surgery, but long-term clinical outcomes have been suboptimal, and many patients still suffer
49 from adverse events[6–9].

50 Another proposed strategy to improve perfusion of the ischemic limb is to stimulate blood
51 vessel growth (therapeutic angiogenesis or revascularization). Medical or cell therapies that deliver
52 VEGF, the main angiogenic growth factor, and other angiogenic growth factors have been developed,
53 but despite great effort, no effective treatment is currently available[10,11]. This is largely due to
54 challenges in the dosing of growth factor delivery, due to our lack of knowledge on how to form
55 *functional* and *perfused* blood vessels in the muscle and due to our limited understanding of the
56 underlying skeletal muscle pathology in PAD[5]. Indeed, microvascular dysfunction is increasingly being
57 reported in PAD, with abnormal microvascular architecture and fibrosis in IC and CLI patients and few
58 studies recently reported partial endothelial-to-mesenchymal transition in PAD patients[12,13] and
59 capillaries of end-stage patients[13] . Also, impaired vasoreactive responses might impair oxygen and
60 nutrient delivery into the ischemic muscle[14]. In this respect, increased vascular density has been
61 observed in some[15–18] but not all[19,20] studies. While the discrepancy underlying these conflicting
62 observations is unclear, persistent ischemia in PAD patients despite increased vascularization
63 nonetheless suggests that an active angiogenic response does not restore microvascular perfusion nor
64 does it resolve tissue ischemia.

65 Several studies using preclinical models of muscle injury have shown that microvascular
66 endothelial cells (ECs) are not only essential for inducing muscle revascularization, but at the same
67 time steer muscle regeneration and tissue repair through their interactions with other cells in the
68 damaged or ischemic muscle microenvironment. ECs induce activation of muscle stem cells[21], control
69 vascular tone through interaction with smooth muscle cells[22] and have strong immune regulatory

70 properties by controlling the entry of immune cells into the tissue, their differentiation into specialized
71 immune effectors as well as (co-)defining the functional properties thereof[23,24]. However, our
72 understanding on how ECs interact with other cell types and might contribute to skeletal muscle
73 pathology in PAD, remains largely unknown.

74 Macrophages are key regulators of muscle regeneration in many settings[25] but also stimulate
75 muscle angiogenesis as well as arteriogenesis in preclinical models of PAD, suggesting that they are
76 key regulators of vascular function[23,26,27]. There is however very limited information on the genetic nor
77 functional properties of macrophages in skeletal muscle from patients suffering from PAD.
78 Inflammatory cytokine profiles of PAD muscle showed that higher levels of inflammatory cytokines
79 correlate with shorter onset claudication pain[28]. In PAD muscle, one manuscript showed that the
80 majority of macrophages express the pro-inflammatory marker CD80 whereas the fraction of
81 regenerative macrophages (using markers such as CD206, CD163 and Arg1) did not differ between PAD
82 patients and healthy controls[29]. In contrast, Kosmac et al[30] reported an increase in the fraction of
83 $CD11b^{+}CD206^{+}$ regenerative macrophages using a histological approach, and those macrophages were
84 positively correlated with fiber size and satellite cell number. On the other hand, less $CD11b^{+}CD206^{-}$
85 inflammatory macrophages was correlated with improved walking performance.

86 In this study, we have applied single cell RNA sequencing (scRNAseq) on muscle samples from
87 PAD patients and non-PAD controls, generating a comprehensive dataset containing over 100,000 cells
88 that provides new insights into the cellular complexity of muscle tissue under both healthy as well as
89 PAD conditions. We confirmed the presence of $ATF3/4^{+}$ ECs[31] with angiogenic and immune regulatory
90 capacities in human muscle and found that their transcriptional profile is profoundly altered during
91 PAD progression. Furthermore, we identified that *LYVE1*^{hi}MHCII^{low} resident macrophages are the
92 dominant macrophage population in human muscle, even under a chronic inflammatory condition
93 such as PAD. This population exhibits a high and active communication with ECs, which is significantly
94 altered in PAD. During PAD, *LYVE1*^{hi}MHCII^{low} macrophages get activated and acquire a more pro-
95 inflammatory profile. We hypothesize that resident macrophage activation could contribute to the
96 chronic inflammatory state observed in PAD[32–34] but their contribution to PAD muscle pathology needs
97 further study.

98

Methods

Patients and study design

Control and PAD patients were recruited from the Department of Angiology, Cantonal Hospital Baden, Baden, Switzerland. The general **inclusion criteria for both control and PAD patients** were: scheduled for surgery (bypass surgery in PAD patients or lower limb aneurysm surgery in control samples); Age ≥45 years; ability to understand German; signed informed consent to participate in the study. **Inclusion criteria specific for PAD patients**: diagnosis of PAD ranging from exercised limited by claudication (Fontaine classification: IIa or IIb) to CLI (Fontaine III-IV); ankle-brachial index (ABI) ≤ 0.90 at rest unless diagnosed with media sclerosis; stable medicament regimen (i.e., statin, anti-platelet, anti-hypertensive regimen). **Inclusion criteria specific for control patients**: diagnosis lower limb aneurysm; ABI > 1 at rest. The general **exclusion criteria for both control and PAD patients** were: severe peripheral neuropathy (Total Neuropathy Score ≥3); unstable angina or severe (>70%) three coronary vessel disease; significant liver dysfunction (Model for End-Stage Liver Disease Score) or known liver cirrhosis (Child-Turcotte-Pugh score >6 points); treated for cancer in the last 2 years; diagnosis of Parkinson's disease. **Exclusion criteria specific for PAD patients**: above/below-knee amputation. **Exclusion criteria specific for control patients**: peripheral artery disease. The study was conducted according to the Declaration of Helsinki, the Human Research Act (HRA) and the Human Research Ordinance (HRO) and the protocol was approved by the Ethics Committee of the Canton of Zurich (KEK number: 2020-01393).

Muscle samples from the medial head of *gastrocnemius* muscle were collected during lower limb aneurysm surgery (control samples) or bypass surgery (PAD samples) and immediately transferred to an ice-cold hypothermic preservation solution (HypoThermosol® FRS Preservation Solution, H4416 Sigma-Aldrich) for optimal transport and conservation until further processing[35]. From 4 PAD and 4 control samples, samples were processed for scRNAseq analysis. An independent set of samples (n= 6 for PAD; n=4 for control) was embedded in optimal cutting temperature medium, frozen in liquid nitrogen-cooled isopentane and stored at -80°C for histological analysis. Transversal 10-µm cryosections of the samples were prepared at -20°C, air dried for ~30 min and stored at -80°C until further processing.

128 ## Isolation of cells from human skeletal muscle for single cell RNA sequencing

129 For isolation of cells for scRNAseq, and in less than 2 hours after collection and preservation in
130 ice-cold hypothermic preservation solution (HypoThermosol® FRS Preservation Solution, H4416 Sigma-
131 Aldrich), samples were minced in a petri dish on ice using scissors and a surgical blade. Minced samples
132 were transferred into a digestion buffer (4 mL digestion buffer per 100 mg of muscle) containing 2
133 mg/ml Dispase II (D4693 Sigma-Aldrich) and 2 mg/ml Collagenase IV (17104019 Thermo Fisher
134 Scientific) in HBSS buffer (14025100 Thermo Fisher Scientific) at 37°C for 25-30 minutes, with gentle
135 shaking every 3-5 minutes. After digestion, the reaction was stopped by adding an equal volume of
136 20% heat inactivated FBS (10500064 Thermo Fisher Scientific) 1mM EDTA (E177 VWR Life Science) in
137 HBSS (14025100 Thermo Fisher Scientific) and the suspension was passed through a 100-µm cell
138 strainer (800100 Bioswisstec) and a 40-µm cell strainer (352340 Falcon). Cell suspension was
139 centrifuged at 500 g for 5 minutes at 4°C and the supernatant discarded. The pellet was resuspended
140 in 1 mL of ACK Lysing Buffer (A1049201 Thermo Fisher Scientific) for red blood cell lysis for 2 minutes
141 at room temperature. After incubation, the reaction was stopped with 4 mL of 10% heat inactivated
142 FBS (10500064 Thermo Fisher Scientific) in HBSS buffer (14025100 Thermo Fisher Scientific). Cell
143 suspension was centrifuged at 500 g for 5 minutes at 4°C and the pellet resuspended in 0.5% BSA
144 (A1391 PanReac AppliChem) in DPBS (14190250 Thermo Fisher Scientific) containing 1mM EDTA (E177
145 VWR Life Science) for FACS. Calcein Violet (65-0854-39 Thermo Fisher Scientific) was added directly to
146 the cell suspension at 1:1000 dilution 10 minutes before sorting.

147 ## Human scRNAseq analysis

148 Metabolically active (Calcein^{+}) human muscle mononuclear cells were FACS sorted and loaded
149 into the 10X Chromium Next GEM Chip G, aiming the recovery of ~10000 cells per sample. scRNAseq
150 libraries were generated according to 10X Chromium Next Gem Single Cell 3' Reagent Kits v3.1
151 (CG000204 Rev D) and sequenced on the Illumina Novaseq 6000 system. We sequenced a total of 13
152 samples from 8 different patients (Table 1). Sequencing reads were aligned to the human genome
153 using CellRanger v5.0.0-7.0.0 and the genome assembly GENCODE GRCh38.p13 Annotation Release
154 37. Intron reads were not included during the alignment. Each individual sample was independently
155 processed for quality control (QC) and log-normalization using *scran* 1.24.1 and *scater* 1.24.0
156 packages[36,37] in R (version 4.2.0). High quality cells were selected based on library size, number of
157 detected genes and percentage of reads mapped to mitochondrial genes, independently adjusting the
158 thresholds for each sample. Raw UMI counts were log-normalized based on library size factors.
159 Doublets were detected and removed in every individual sample using the default parameters of the
160 function *runDoubletFinder* from *singleCellTK* 2.6.0 package[38]. After individual QC and log-

161 normalization, all samples were batch-corrected and merged using *Harmony* 0.1.1 package[39].
162 Dimensionality reduction by t-Distributed Stochastic Neighbor Embedding (TSNE) was performed
163 based on the dimensions generated by *Harmony* integration. Clustering was performed by building a
164 nearest neighbor graph (k = 20) and then applying the Louvain algorithm as implemented in *Seurat*
165 4.1.1 package[40]. For individual analysis and reclustering of the EC and monocyte/macrophage
166 populations, cells were selected by tracing back the clustering of the complete dataset in every
167 individual sample. Raw counts from selected cells, either ECs or monocyte/macrophage, were log-
168 normalized in every individual sample and batch-corrected and merged as described above for the
169 complete dataset. All dotplots showing gene expression were generated using the *plotDots()* function
170 as implemented in scater 1.24.0 package. Cell type proportions in each condition were calculated by
171 dividing the number of cells in each cluster by the total number of cells in that respective condition.

172 Differentially expressed genes (DEGs) were detected by performing a Wilcoxon Rank Sum test
173 as implemented in *Seurat* 4.1.1 package. DEGs were selected based on a minimum $\log_2$ fold change of
174 0.25 and an adjusted p-value < 0.05. For over-representation analysis (ORA), selected DEGs were
175 ordered based on increasing adjusted p-value and given as an input in the web-based implementation
176 of g:Profiler[41], selecting the option "Ordered query" before running the analysis. ORA results were
177 represented as the -log10 of the p-values obtained for each process. ORA analysis results were
178 simplified by using *rrvgo* 1.10.0 package[42]. Redundant terms were grouped and only the most
179 significant term of each group was conserved. Schematic visualization of KEGG pathways from ORA
180 results were generated using *pathview* 1.38.0 package[43].

181 For pseudobulk analysis, lowly expressed genes were removed if they were not detected in at
182 least 10 cells. Raw UMI counts were aggregated per patient (total sum of counts for every gene from
183 all cells in every patient). For differential expression analysis in the pseudobulk dataset, we applied
184 *DESeq2* 1.38.3 package[44] and performed the comparison between control and PAD patients. All
185 significant DEGs (adjusted p-value <0.05) were reported in a heatmap (Figure 1J) by using the
186 normalized counts (by size factors) in each patient and scaled and centered based on gene expression
187 per patient. For Gene Set Enrichment Analysis (GSEA) in the pseudobulk dataset we applied *fgsea*
188 1.24.0 package[45]. From the differential expression analysis results performed with DESeq2 we selected
189 the *stat* value (Wald statistic: the log2FoldChange divided by lfcSE) for each gene and performed GSEA
190 analysis using the default settings of *fgsea()* function from *fgsea* 1.24.0 package. Significant pathways
191 were selected based on an adjusted p-value < 0.05. Human Hallmark pathways from MsigDB[46] were
192 used for this analysis.

193 Gene Set Variation Analysis was performed using *GSVA* 1.46.0 package[47]. Log-normalized

194 counts from the corresponding scRNAseq dataset (either ECs or Monocytes/Macrophages) were given
195 as an input for the *gsva()* function as implemented in GSVA 1.46.0 package. The gene sets to perform
196 GSVA were obtained from Fan et al[31] (ATF4 dependent genes as defined by genes with logFC < -0.1 and
197 adjusted p-value < 0.05 after comparing mouse muscle ECs in wild-type and EC-specific inducible ATF4
198 knockout mice) or Sanin et al[48] (macrophage activation processes). For GSVA of M1-M2 signatures, we
199 obtained the genesets from Varga et al[49], which reported a set of M1-M2 genes derived from *in vitro*
200 stimulation and generated genesets for pro-inflammatory (Ly6C$^+$) and pro-regenerative (Ly6C$^-$)
201 macrophages at different timepoints after cardiotoxin-induced muscle injury.

202 Bulk RNAseq data from muscle ECs in WT and EC-specific ATF4 KO mice were obtained from
203 Fan et al[31] and processed as described by the authors. Only WT and ATF4 KO red muscle ECs (RmECs)
204 were used in this study.

205 Transcription factor inference analysis was performed using the Python implementation of
206 SCENIC package (pySCENIC)[50,51] and following the script provided by the authors in their GitHub
207 repository (https://github.com/aertslab/pySCENIC). Cell communication analysis on the complete
208 dataset (all cell types in control and PAD samples) was performed using *CellChat* 1.6.1 package[52]
209 following the script provided by the authors in their GitHub repository (*Full tutorial for comparison*
210 *analysis of multiple datasets* section in https://github.com/sqjin/CellChat). Cell communication
211 analysis between ATF3/4$^+$ ECs and *LYVE1*^{hi}MHCII^{low} macrophages was performed using *nichenetr* 1.1.0
212 package[53] following the script provided by the authors in their GitHub repository (*Differential NicheNet*
213 *analysis between conditions of interest* section in https://github.com/saeyslab/nichenetr).

214 All raw and processed (10X CellRanger output files) sequencing data are available at
215 GSE235143.

216 Tissue Immunofluorescence and Histology

217 Human muscles were harvested and embedded in OCT embedding matrix (6478.1, Carl Roth)
218 and frozen in liquid N_2-cooled isopentane. Frozen sections (10 µm) were made using a cryostat (Leica
219 CM 1950). The following antibodies were used: anti-LYVE1 (1:200 dilution, ab33682, Abcam), anti-
220 CD68 (1:100 dilution, ab955, Abcam), anti-CD31 (1:200 dilution, M082329-2, Dako), Goat anti-Rabbit
221 IgG Cross-Adsorbed Secondary Antibody, Alexa Fluor 568 (1:200 dilution, A-11001, Thermofisher),
222 Goat anti-Mouse IgG Cross-Adsorbed Secondary Antibody, Alexa Fluor 488 (1:200 dilution, A-1101,
223 Thermofisher), Alexa Fluor 647 conjugated wheat germ agglutinin (WGA, 1:50 dilution, W32466,
224 ThermoFisher). Muscle sections were fixed in 4% paraformaldehyde (PFA) followed by epitope
225 retrieval using sodium citrate (10 mM, pH 6.5) at 92 °C for 20 min. Endogenous peroxidase activity was

226 blocked with 3% hydrogen peroxide in phosphate-buffered saline followed by 10 min of
227 permeabilization (PBS + 0.5% Triton X-100) and 60 min of blocking at room temperature in blocking
228 buffer (PBS + 1% BSA). After blocking, sections were stained overnight at 4°C with primary antibodies,
229 followed by 1 hour incubation of secondary antibodies at room temperature. Extracellular matrix was
230 stained using wheat germ agglutinin (WGA). Nuclei were detected using Hoechst diluted 1:5000 in PBS
231 and for 5 minutes at room temperature. Slides were then washed with PBS and mounted using Immu-
232 Mount (9990412, Thermofisher). Slides were imaged on an AxioObserver.Z1 fluorescence microscope
233 using a 20x and 40x objective (Carl Zeiss, Oberkochen, Germany). For the LYVE1 and CD68 staining,
234 315 ± 106 (mean ± standard deviation [SD]) fibers were counted per patients, and for the CD31
235 staining, 409 ± 80 (mean ± SD) fibers were counted. Different regions over the whole tilescan muscle
236 section were analyzed with the Zen software (ZEN 2011 imaging software, Zeiss) and Fiji. General tissue
237 morphology was evaluated using haematoxylin and eosin (H&E) staining. H&E images were acquired
238 with an Eclipse Ti2 inverted microscope (Nikon) using a 20x objective.

239 **Statistics**

240 The histology images presented in the manuscript are representative of the data
241 (quantification of images is approximately the group average) and the staining quality. All imaging data
242 are represented as violin plots, where the three horizontal lines represents the median and quartiles,
243 and the width of the plot indicates the distribution of the data. GraphPad Prism software (version
244 9.2.0) was used for statistical analyses. Shapiro-Wilk test was performed to analyze data distribution.
245 Non-normally distributed data were analyzed by non-parametric Mann-Whitney U test to compare
246 two groups. Normally distributed data were analyzed using Student's t-test in an unpaired two-tailed
247 fashion to compare two groups. $P > 0.05$ is considered non-significant (ns).

248 # Results

249 ## scRNAseq reveals a high degree of cellular heterogeneity in human skeletal muscle

250 To investigate the cellular landscape of patients who have been diagnosed with PAD, we
251 collected samples from the medial head of the *gastrocnemius* muscle of individuals undergoing either
252 lower limb aneurysm surgery (controls) or PAD bypass surgery (PAD) (see Methods). A subset of patient
253 samples was used for scRNAseq (4 control vs 4 PAD) while an independent subset was frozen down for
254 histological analysis (4 control vs 6 PAD (Figure 1A, Table 1). Histological evaluation revealed that
255 myofiber size nor diameter was affected in PAD patients (Figure 1B-D). Also, we did not observe signs
256 of muscle necrosis nor regenerating fibers characterized by centrally localized nuclei. Since there have
257 been conflicting observations with some studies reporting reduced[19,20] or higher[15–18] vascular density
258 in PAD, we also stained for $CD31^+$ ECs and found increased vascular density in our specific cohort
259 (Figure 1E-F).

260 To obtain better insight into the molecular characteristics of PAD muscle, we performed
261 scRNAseq in an independent subset of patients (Table 1). Those samples were processed for tissue
262 digestion, and metabolically active mononuclear cells ($Calcein^+$) were isolated using fluorescence
263 activated cell sorting (FACS). Sorted cells were then loaded into the 10X Chromium technology to
264 perform scRNAseq (Figure 1A). Following sequencing, each individual sample underwent quality
265 control (QC) filtering to select high quality cells, and raw counts were log normalized. The resulting QC
266 filtered and log normalized samples were pooled together and batch corrected. The final dataset was
267 comprised of 106,566 high-quality, deep-sequenced cells, as indicated by an average of 2359 genes
268 detected per cell and an average of 10.84% of reads mapped to mitochondrial genes. After initial
269 bioinformatic analysis, clustering, and t-Distributed Stochastic Neighbor Embedding (TSNE) we
270 detected 9 major cell populations (Figure 1G). As revealed by unbiased marker gene detection, the
271 dataset comprised heterogeneous and defined cell populations that we manually annotated based on
272 the expression of well-known marker genes[54–56] (Figure 1H). We still detected approximately 10-15%
273 of myonuclei, similar to other datasets[57,58], but our dataset was nicely enriched for mononuclear cells.
274 We identified the main cell types found in skeletal muscle, including several immune cell populations
275 (macrophages/monocytes, mast cells, neutrophils, NK/T/B cells), endothelial cells (ECs), mural cells
276 (smooth muscle cells (SMCs)/pericytes), stem cells (fibro-adipogenic progenitors (FAPs), and muscle
277 stem cells (MuSCs)/satellite cells). All cell types were present in both control and PAD patients and no
278 obvious differences in the fractional contribution of a cell type to the overall sample were detected
279 between groups (Figure 1I).

280 To get insight into the general transcriptional differences between conditions, we compared
281 the transcriptomes of all patients by a pseudobulk analysis[59]. As shown in Figure 1J (and Supplemental
282 File 1), control and PAD samples were separated in two distinct clusters based on differential
283 expression of the top high variable genes in the dataset, showing a clear differential transcriptomic
284 signature between both conditions. Gene Set Enrichment Analysis (GSEA) using Hallmark pathways[46]
285 over this comparison revealed an increase in tumor necrosis factor alpha (TNFA) signaling and
286 interleukin-6 (IL6) signaling, both associated with poor prognosis and reduced walking performance in
287 PAD patients[60,61] (Figure 1K). Beyond inflammatory processes, GSEA also showed higher enrichment
288 score of several metabolic pathways such as oxidative phosphorylation, glycolysis and mTORC1
289 signaling in PAD patients, while bile acid metabolism was repressed (Figure 1K). Interestingly, several
290 of the identified pathways such as the inflammatory activation, unfolded protein response and
291 metabolism were also differentially regulated in previously published bulk RNAseq experiments of PAD
292 muscle[62,63]. In contrast to our mononuclear single cell approach, those bulk tissue datasets are
293 commonly dominated by myonuclear gene pools, typically >70% of nuclei in skeletal muscle are of
294 myonuclear origin[64], thus suggesting that common pathways might be affected in different cell types.

295 Our initial clustering (Figure 1G) only partially addressed the high degree of heterogeneity of
296 the dataset and provided a significant source for exploration of the molecular differences between
297 PAD and control samples, thereby potentially unravelling molecular mechanisms involved in PAD
298 progression. All transcriptomic data are made available for download (GEO Accession Code:
299 GSE235143). Moreover, further subcellular clustering will identify many subpopulations within each
300 major cell type. For the purpose of this manuscript, we decided to conduct a comprehensive analysis
301 on ECs and macrophages because of their crucial role in angiogenesis, inflammation, and tissue repair,
302 which are key factors in the pathogenesis and progression of PAD[29,65,66].

303 Human skeletal muscle contains ATF3/4^{+} endothelial subpopulations with 304 immunoregulatory capacities

305 Using our initial clustering, we selected ECs from every individual QC filtered and log
306 normalized sample. Following the same approach we used for the complete dataset, we batch
307 corrected and pooled all the samples together. The dataset comprised 14355 high-quality ECs with an
308 average of 2120 genes detected per cell and an average of 10.54% of reads mapped to mitochondrial
309 genes. Clustering and TSNE projection revealed 6 different EC clusters (Figure 2A). Previous scRNAseq
310 studies in skeletal muscle[31,67] have established marker genes for the main EC types (arteries, capillaries,
311 veins, and lymphatic ECs) which we used to annotate the EC populations (Figure 2B). Additionally,
312 unbiased marker gene detection revealed specific gene sets for every individual population,

313 demonstrating that we identified well defined EC subtypes (Figure 2C and Supplemental File 1). Our
314 clustering however revealed two distinct populations of venous and capillary ECs that could not be
315 distinguished by general endothelial markers (Figure 2B) but clearly separated in the TSNE graph and
316 in the marker gene heatmap (Figure 2A,C). Interestingly, differential expression analysis between both
317 venous clusters detected a common set of genes significantly upregulated in venous 1 and capillary 1
318 populations but not in the other EC subtypes (Figure S1A). For a functional characterization of these
319 venous 1 and capillary 1 populations, we then performed an over-representation analysis (ORA)[41] to
320 identify the main processes in which these genes are involved. Interestingly, the top enriched pathways
321 identified by the ORA analysis using the KEGG pathway database[68] yielded a collection of processes
322 that have previously been linked to recruitment and functional modulation of immune cells by ECs
323 including TNF signaling, IL-17 signaling and NF-kappa B signaling pathways[24,69,70] as well as a lipid and
324 atherosclerosis signaling (Figure 2D). A deeper analysis of the TNF signaling and lipid and
325 atherosclerosis signaling pathways revealed that the upregulated genes in these ECs are immune
326 regulatory genes directly involved in leukocyte recruitment, leukocyte activation, cell adhesion and
327 cytokine signaling (Figure S1B-C).

328 ORA analysis for transcription factor (TF) motif enrichment identified ATF4 as a top TF
329 regulating the expression of these genes (Figure 2E). In a prior study, we identified a subpopulation of
330 *Atf3/4*$^{+}$ muscle ECs in mouse using scRNAseq and subsequently found that ATF4 is functionally relevant
331 by showing its requirement for exercise-induced angiogenesis by controlling a set of genes involved in
332 amino acid uptake and metabolism[31]. Similarly, ATF3 is required for regeneration of the aortic
333 endothelium[71]. First, direct comparison of the marker genes defining the mouse *Atf3/4*$^{+}$ subpopulation
334 based on the scRNAseq experiment with the current human dataset showed that those were highly
335 enriched in both the venous 1 and capillary 1 clusters from human skeletal muscle (Figure S1D). In our
336 previous work, we also performed a bulk RNAseq experiment in ECs isolated from mouse skeletal
337 muscle of wild type and EC-specific inducible ATF4 knockout (KO) mice. This experiment revealed a
338 specific set of endothelial ATF4-dependent genes that were downregulated upon EC-specific loss of
339 ATF4[31]. When mapping this ATF4-dependent gene set against the genes that we found upregulated in
340 the identified human venous 1 and capillary 1 clusters (Figure S1A), we noticed that the majority
341 thereof were controlled by ATF4 (Figure S1E). We also used the ATF4-dependent gene set to perform
342 gene set variation analysis (GSVA)[72] which calculates a score for each cell based on the expression
343 levels of an input gene set (e.g. ATF4-dependent genes) relative to the whole transcriptome of the cell.
344 Within our human dataset, the ATF4-dependent GSVA score was higher for venous 1 and capillary 1
345 clusters compared to the other clusters (Figure 2F). Furthermore, we performed unbiased TF regulator
346 network inference using SCENIC[50,51] which generates a *TF regulon activity score* for each cell based on
347 the coexpression of TFs and their target genes that are identified by the presence of TF binding motifs

348 in their promoter regions. SCENIC revealed that ATF4-dependent transcription factors (such as ATF3,
349 FOS, FOSB, JUN, JUNB and JUND) (Figure S1E) showed the highest transcriptional activity in ECs and
350 their regulons were specifically active in venous 1 and capillary 1 clusters (Figure S1F). In conclusion,
351 venous 1 and capillary 1 populations are ATF3/4$^+$ ECs and we thus annotated these populations as
352 ATF3/4$^+$ venous ECs and ATF3/4$^+$ capillary ECs. Interestingly, when looking at the fractional
353 contribution of EC subpopulations, we found a reduced fraction of ATF3/4$^+$ capillaries in PAD samples
354 when compared to control (Figure 2G), suggesting that these cells could contribute to the progression
355 of the disease.

356 **ECs undergo profound transcriptomic rewiring during PAD**

357 Next, we assessed whether the different EC populations showed transcriptomic changes
358 between control and PAD samples. Therefore, we calculated the number of genes that are
359 differentially expressed between conditions for each individual population and, at the same time,
360 specific for that cluster compared to the rest (Figure 2H and Supplemental File 1). Both ATF3/4$^+$ venous
361 and capillary ECs showed the highest number of differentially expressed genes between control and
362 PAD samples (Figure 2I) indicating that these two populations are profoundly modifying their
363 transcriptome during PAD progression. To further investigate the transcriptomic switch in PAD samples
364 at the pathway level, we selected genes that were up- or downregulated in both ATF3/4$^+$ venous as
365 well as capillary ECs (Figure S2A and Supplemental File 1) and performed an ORA analysis using the
366 *biological process* category from the Gene Ontology (GO) database[73,74]. Interestingly, while few of
367 enriched processes were activated in the PAD ATF3/4$^+$ populations (Figure S2B and Supplemental File
368 1), most of them were downregulated indicating that many of the biological functions exerted by the
369 ATF3/4$^+$ ECs are repressed during the progression of PAD. The PAD populations showed an increase in
370 processes related to platelet activation and wound healing (Figure 2J). Although these results suggest
371 that ATF3/4$^+$ ECs are actively trying to induce a regenerative response, it is likely not effective as they
372 at the same time downregulated many processes related to angiogenesis, immune regulatory
373 functions, interaction with leukocytes as well as metabolism (Figure 2J and S2C). Also, ATF3/4$^+$ ECs
374 upregulated a set of genes related to the cellular response to metal ions such as cadmium, copper, and
375 zinc in PAD samples (Figure 2J). This is interesting since several studies have confirmed elevated levels
376 of these ions in the blood and urine of patients with PAD and atherosclerotic lesions, suggesting they
377 might be risk factors for the disease[75–79], and have linked those to endothelial dysfunction[80–82] .

378 The activation of epithelial-to-mesenchymal transition in ATF3/4$^+$ capillary ECs (Figure 2J)
379 prompted us to investigate whether capillary ECs undergo Endothelial-to-mesenchymal (EndoMT) in
380 PAD. Recent manuscripts reported abnormal microvascular architecture with increased perivascular
381 collagen deposition[13]. Increased markers of EndoMT were also reported in a fraction of the small

382 arterioles in CLI patients, likely due to increased TGB signaling via pericytes[12]. Focusing on capillary ECs,
383 we noticed a characteristic EndoMT pattern, as described in Tombor *et al.*[83], which includes the
384 downregulation of fatty acid transport and metabolism genes versus the partial activation of a
385 mesenchymal signature (Figure 2K). Interestingly, some 'canonical' EndoMT genes like *SNAI1, S100A4*
386 and *SERPINE1* were not affected in PAD while several genes related to extracellular matrix (ECM)
387 composition, such as *COL1A1*, *COL1A2* and *FN1* were highly upregulated (Figure 2K). This phenotype
388 was present in both capillary subpopulations but was more pronounced in the ATF3/4^{-} ECs (annotated
389 as Capillary). Also, capillary ECs from PAD patients lowered CDH5 expression but did not completely
390 lose it (Figure S2D), suggesting that they at least partially undergo EndoMT. Because of the strong
391 activation of ECM genes, we investigated how ECs in PAD rewire their matrisome, a set of genes that
392 define ECM composition and function[84]. Capillary ECs in PAD only changed 11.7% (32/274) of the core
393 matrisome genes, but showed significant activation of specific ECM genes such as collagens, *FN1,*
394 *FBN1,* as well as alterations in components of the basement membrane such as laminins, *HSPG2*
395 (perlecan), and *NID2* (nidogen) (Figure 2L). Taken together, ECs in PAD undergo profound
396 transcriptomic alterations that impair immune regulatory functions but promote EndoMT.

397 LYVE1^{hi}MHCII^{low} resident macrophages are the dominant macrophage population in 398 PAD

399 Blood vessel formation and remodeling is heavily influenced by resident and recruited cells. In
400 experimental models of PAD, monocyte-derived macrophages contribute to arteriogenesis as well as
401 angiogenesis[11,23,26,27,29,65,85]. Macrophages also control muscle regeneration: under settings of acute
402 muscle ischemia or muscle damage, they initially have a pro-inflammatory M1-like phenotype, which
403 is associated with the expression of several cytokines that further promote inflammation[86]. Rapidly
404 thereafter, those M1-like macrophages repolarize and change their phenotype towards an anti-
405 inflammatory restorative/regenerative M2-like phenotype[86–88]. This M1- to M2-like repolarization is
406 required for optimal muscle regeneration[87,89,90]. M2-like macrophages also have an important pro-
407 angiogenic role since they are a main source of VEGF. Preventing macrophage infiltration in the injured
408 muscle is also associated with decreased angiogenesis[91] and inhibiting M2-like macrophage
409 polarization fails to remodel collateral arteries and to induce angiogenesis following ischemic
410 damage[92]. However, acute mouse models do not reflect the chronic pathophysiology of PAD, so the
411 contribution of macrophages to human PAD is poorly understood. We thus decided to further
412 investigate the Monocytes/Macrophages cluster (MoMac). Similar to our approach with ECs, we
413 selected MoMac cells from each QC filtered and log normalized sample, performed batch correction,
414 and merged them. The final dataset was comprised of 10783 high-quality MoMac cells as indicated by
415 an average of 2743 genes detected per cell and an average of 11.94% of reads mapped to

416 mitochondrial genes. Clustering and TSNE revealed 5 distinct clusters (Figure 3A). Previous research
417 has established an extensive set of marker genes for different MoMac populations[93–96] that allowed us
418 to clearly annotate the different populations in our dataset (Figure 3B). Unbiased marker gene
419 detection confirmed that we identified well defined macrophage and monocyte populations (Figure
420 3C and Supplemental File 1). The dataset was comprised of classical monocytes (cMonocytes),
421 *CD16*(*FCGR3A*)$^{+}$ monocytes, dendritic cells (DCs) and two macrophage populations. Alternatively, we
422 could also classify the two monocytes and DC populations as CCR2^{+}CX3CR1^{low}CD14^{hi}CD16^{low}
423 (cMonocytes and DCs) and CCR2^{-}CX3CR1^{hi}CD14^{low}CD16^{hi} (CD16^{+} Monocytes) (Figure S3A). The
424 CD14^{hi}CD16^{low} and CD14^{low}CD16^{hi} human monocyte populations are the equivalent to Ly6C^{hi} and
425 Ly6C^{low} monocytes in mice, respectively[97]. Ly6C^{hi} monocytes are recruited monocytes that rapidly
426 infiltrate the tissue upon injury or infection[98] while Ly6C^{low} cells are patrolling monocytes that crawl on
427 the inside of blood vessels onto endothelial cells and only extravasate in response to tissue damage or
428 infection after which they differentiate into macrophages[99].

429 The macrophage subpopulations were characterized by different expression levels of *LYVE1*
430 and genes of the Major Histocompatibility Complex Class II (MHCII), and therefore annotated as
431 *LYVE1*^{hi}MHCII^{low} macrophages and *LYVE1*^{low}MHCII^{hi} macrophages (Figure S3B). Both populations have
432 previously been identified[100] in various tissues as *LYVE1*^{hi}MHCII^{low}*CX3CR1*^{low} and
433 *LYVE1*^{low}MHCII^{hi}*CX3CR1*^{hi}, which is consistent with our dataset (Figure S3B)[100]. *LYVE1*^{hi} and *LYVE1*^{low}
434 macrophages derive from different origins[101], with the former being tissue-resident macrophages
435 which are seeded in the tissue during embryonic development and locally self-renew throughout life
436 while the latter are mainly derived from recruited monocytes during adulthood. Additionally,
437 *LYVE1*^{hi}MHCII^{low} macrophages have a perivascular localization[100], but how they interact with blood
438 vessels is poorly studied. Consistent with literature, *LYVE1*^{hi}MHCII^{low} macrophages in our human
439 muscle samples expressed high levels of tissue-resident macrophage marker genes including *LYVE1*,
440 *FOLR2*, *CD209*, *MERTK*, *SELENOP*, *STAB1* and *MAF*[94–96], confirming that those are resident macrophages
441 (Figure 3B). As expected, *LYVE1*^{hi} macrophages were the largest population in the control samples,
442 accounting for 70 ± 6% of the MoMac dataset (Figure 3D). And even though the fractional contribution
443 of *LYVE1*^{hi} resident macrophages was slightly lower in PAD samples, they still remained the largest
444 population (40 ± 3% of the PAD MoMac dataset). Immunostainings for LYVE1 in combination with the
445 pan-monocyte/macrophage marker CD68 confirmed the dominant fractional contribution of *LYVE1*^{hi}
446 resident macrophages in human muscle, both under control as well as PAD settings (Figure 3E-F)
447 despite a clear increase in the number of CD68^{+} monocyte/macrophages in PAD (Figure 3G), consistent
448 with previous work[29]. We did however not observe a reduction in the fraction of *LYVE1*^{hi}*CD68*$^{+}$ cells,
449 likely due to thresholding differences or potential differences in cell size. Finally, in our scRNAseq

450 dataset, the fraction of cMonocytes, but not monocyte-derived *LYVE1*^{low} macrophages, went up in PAD
451 (Figure 3D), suggesting that monocyte-to-macrophage differentiation is impaired in PAD.

452 Macrophages and monocytes are heterogeneous cells with a wide range of functionalities
453 depending on the tissue environment and type of stimuli. Sanin et al[48] established a framework for
454 macrophage activation by analyzing macrophage heterogeneity across different tissues and
455 inflammatory conditions and reported a set of common initial and early stages of macrophage
456 activation that further divided into different functional categories defined as phagocytic, oxidative
457 stress, inflammatory or remodeling (regenerative) paths. We utilized this framework to characterize
458 the functional differences between the MoMac populations in our dataset. Classical monocytes, CD16^{+}
459 Monocytes and DCs shared a set of common processes related to an early stage of activation including
460 ECM and actin regulation, cytoskeleton organization and ECM-receptor interaction (Figure 3H).
461 Additionally, these cells showed processes related to the inflammatory and oxidative stress paths
462 including innate immune responses and phagosome, respectively (Figure 3H). Interestingly, only
463 *LYVE1*^{low} macrophages, along with DCs, showed a profile of antigen presentation, in line with their
464 higher MHCII levels (Figure S3B) and consistent with previous characterization of these cells[100]. Both
465 *LYVE1*^{hi} and *LYVE1*^{low} macrophages were characterized by a specific phagocytic profile as they showed
466 processes related to this path including complement signaling, phagocytosis, coagulation cascades and
467 regulation of myeloid leukocyte differentiation. Interestingly, Sanin et al[48] reported that phagocytic
468 path macrophages are the dominant population in a dataset from mouse aorta atherosclerotic
469 plaques[102] and interventions promoting plaque regression accelerated the transit of macrophages
470 along the phagocytic path[48].

471 The function and contribution of resident macrophages in muscle upon loss of muscle
472 homeostasis, and in particular in PAD, is poorly understood. Moreover, no genetic data exploring the
473 transcriptional changes of these cells upon loss of muscle homeostasis are available. We thus decided
474 to further explore whether resident *LYVE1*^{hi} and monocyte-derived *LYVE1*^{low} macrophages exhibit
475 features corresponding to the pro-inflammatory (M1) versus alternative pro-regenerative
476 macrophages (M2)[103,104]. We used published gene sets associated with M1 or M2 polarization[49] under
477 *in vitro* (LPS+IFN-γ (M1) versus IL-4 (M2) stimulation). Since those do not properly reflect the *in vivo*
478 functional polarization state, we also used gene sets from macrophages that were isolated from
479 skeletal muscle upon cardiotoxin injury[49] (Ly6C^{+} at day 2 after injury are pro-inflammatory (M1-like)
480 macrophages whereas Ly6C^{-} at day 4 after injury are pro-regenerative (M2-like) macrophages). GSVA
481 using these gene sets showed that *LYVE1*^{hi} resident macrophages expressed lower levels of both
482 M1/inflammatory as well as M2/regenerative related genes (Figure 3I), consistent with their proposed
483 'homeostatic' function. Additionally, *LYVE1*^{low} monocyte-derived macrophages showed higher

484 expression of both M1 and M2 signatures, as shown in previous studies that report hybrid phenotypes
485 of *in vivo* macrophages[105], although they exhibited a more pronounced pro-inflammatory M1 signature
486 (Figure 3I). Thus, *LYVE1*^{hi} resident macrophages do not reflect the genetic fingerprint of
487 M1/inflammatory nor M2/regenerative macrophages.

488 LYVE1^{hi}MHCII^{low} macrophages get activated during PAD by increasing their 489 inflammatory and migratory responses

490 To assess whether the transcriptomic profiles of the MoMac populations are altered upon PAD,
491 we detected the differentially expressed genes between conditions for every individual population and
492 observed significant alterations in gene expression across all MoMac populations during PAD
493 progression (Figure 3J-K and Supplemental File 1). However, since the role of perivascular resident
494 muscle macrophages is poorly understood, and because it comprises the dominant macrophage
495 population, even in PAD muscle, we specifically focused on the resident *LYVE1*^{hi}MHCII^{low} macrophages
496 where a considerable set of genes was activated in PAD, but we also detected several downregulated
497 genes (Figure S3C and Supplemental File 1). We performed ORA analysis on the DEG between control
498 and PAD *LYVE1*^{hi}MHCII^{low} macrophages (Figure S3D and Supplemental File 1) and found that most of
499 the enriched biological processes were associated with the genes upregulated during PAD (Figure S3D).
500 The top enriched processes in PAD *LYVE1*^{hi}MHCII^{low} macrophages were mainly associated with cell
501 migration, inflammatory and immune responses, increased cytokine production and macrophage
502 activation (Figure S3E), suggesting that resident *LYVE1*^{hi}MHCII^{low} macrophages get activated in PAD.
503 *CCL18*, *NAMPT* and *CCL3* were the top upregulated cytokines in *LYVE1*^{hi}MHCII^{low} macrophages during
504 PAD. High expression of these cytokines has been detected in atherosclerotic lesions and patients with
505 cardiovascular diseases[106–109] with *NAMPT* and *CCL3* having an active role in atherosclerotic plaque
506 formation[110,111], but a role in skeletal muscle of PAD has not been studied. Interestingly, the top
507 repressed processes in PAD were related to heat responses and protein folding (Figure S3E). ORA
508 analysis revealed that the heat shock proteins *HSPA1A* and *HSPA1B* were the main drivers for the
509 repressed processes. *HSPA1A* and *HSPA1B* have been associated with atheroprotective and anti-
510 inflammatory roles in macrophages[102,112,113], and the loss of this anti-inflammatory role in PAD is
511 consistent with the activation of inflammatory processes. Altogether, resident *LYVE1*^{hi}MHCII^{low}
512 macrophages get activated and acquire pro-inflammatory properties during PAD.

513 Endothelial-macrophage crosstalk modifies the functional properties of 514 LYVE1^{hi}MHCII^{low} macrophages during PAD

515 To study the origin and strength of cellular communication networks within the muscle
516 microenvironment, we subsequently applied CellChat[52] in the complete dataset. CellChat revealed a

517 complex communication network between all the cell types (Figure 4A), but while the number of
518 interactions did not change between control and PAD (Figure 4A), the interaction weight, defined as
519 the communication probability based on ligand-receptor pairs expression, was reduced in PAD (Figure
520 4B). Focusing on ECs, they had more interactions in PAD (Figure 4C), specifically with other components
521 of the vascular niche such as FAPs, monocytes/macrophages and smooth muscle cells/pericytes,
522 although the strength of these interactions was slightly reduced (Figure 4D). Monocytes/macrophages
523 showed the highest increase in the interaction strength during PAD, particularly with neutrophils.
524 When analyzing all outgoing and incoming signaling, FAPs were the main senders in the muscle
525 whereas ECs, monocytes/macrophages, NK/T/B cells and smooth muscle cells/pericytes were the main
526 receptors for ligands (Figure 4E). In PAD, the overall outgoing and incoming signals were reduced,
527 although monocytes/macrophages and ECs remained the top receivers. Next, we analyzed which
528 signaling networks were altered between control and PAD. As expected, most pathways were reduced
529 in PAD (Figure 4F). However, pro-inflammatory IL1 signaling was one of the top enriched pathways in
530 PAD samples. On the other hand, MHC-II signaling was one of the top signaling pathways reduced in
531 PAD (Figure 4F). Monocytes/Macrophages were the main receiver of these ligands whereas ECs were
532 the main senders (Figure 4G). Additionally, VEGF signaling was also reduced in PAD (Figure 4H), with
533 ECs as the specific receiver of this communication. The reduction of MHC-II and VEGF signaling in ECs
534 is consistent with the loss of immune regulatory and angiogenic properties of ATF3/4^{+} ECs in PAD
535 (Figure 2J).

536 Finally, to gain a better understanding on how EC-macrophage interactions are affected in PAD
537 at a deeper level, we selected both cell types from our initial clustering (Figure 1G) in every individual
538 QC filtered and log normalized sample. After pooling and batch correcting all the samples, we applied
539 the individual clustering of ECs and MoMac datasets (Figure 2A and 3A) to the combined dataset. We
540 applied NicheNet[53] to predict ligand-receptors pairs that are both differentially expressed and active
541 between control and PAD samples. Compared to CellChat, NicheNet can additionally link the ligand-
542 receptor pairs to the (in)activation of their downstream targets, and thus infer signaling activity, by
543 taking advantage on prior knowledge on signaling and gene regulatory networks. We focused on
544 identifying which ligands expressed by ATF3/4^{+} venous and capillary ECs are recognized by receptors
545 expressed on *LYVE1*^{hi}MHCII^{low} macrophages. Strikingly, NicheNet identified a set of ligand-receptor
546 pairs specifically upregulated in control samples (Figure 5A) as well as a completely different set
547 upregulated in PAD samples (Figure 5B), indicating a profound rewiring of the communication network
548 between ATF3/4^{+} ECs and *LYVE1*^{hi}MHCII^{low} macrophages in PAD. Some of the top reduced signals
549 during PAD were related to GAS6 and CSF1 signaling networks (Figure 5A). Interestingly, CSF1 is the
550 primary growth factor responsible for macrophage differentiation, survival, and proliferation[114], and
551 endothelial CSF1 contributes to macrophage differentiation[115]. Furthermore, inhibition of GAS6

552 signaling in macrophages increases their inflammatory responses and cytokine production[116,117].
553 Inhibition of GAS6 would be consistent with the activated state of *LYVE1*^{hi}MHCII^{low} macrophages in
554 combination with their increased cytokine production (Figure S3E). On the other hand, some signaling
555 networks were enriched during PAD including IL6 signaling (Figure 5B), which has classically been
556 associated with pro-inflammatory functions, but several studies also indicated an anti-inflammatory
557 and atheroprotective role for IL6[118,119]. These results further highlight a complex communication
558 network between ATF3/4^{+} ECs and *LYVE1*^{hi}MHCII^{low} macrophages, which is profoundly altered during
559 PAD.

560 We also used NicheNet to detect which significantly upregulated genes in *LYVE1*^{hi}MHCII^{low}
561 macrophages during PAD could be downstream targets of ligands produced by ATF3/4^{+} ECs (Figure 5C).
562 These target genes included *CCL18*, *SGK1*, *PLAUR*, *CCL3*, *LMNA*, *HBEGF*, *IGFS6*, *FTH1* and *CTSB* (Figure
563 5C). An ORA analysis on these target genes predicted their association with migration, cytokine
564 response, inflammatory response, and immune related processes (Figure 5D). Since we already
565 showed that *LYVE1*^{hi}MHCII^{low} macrophages significantly upregulate genes that are associated with
566 migration, cytokine signaling, inflammatory and immune responses (Figure S3E), the results from this
567 cell communication analysis indicate that the ligands expressed by ATF3/4^{+} ECs during PAD might play
568 a role in the activation of *LYVE1*^{hi}MHCII^{low} macrophages.

569 In conclusion, cellular crosstalk in the muscle microenvironment is significantly affected in
570 PAD. For instance, high and active communication between ATF3/4^{+} ECs and *LYVE1*^{hi}MHCII^{low}
571 macrophages is considerably altered in a PAD context and some of the ligands produced by ATF3/4^{+}
572 ECs could be directly involved in macrophage activation during PAD by modulating signaling networks
573 related to migration, cytokine signaling and inflammation.

574 ## Discussion

575 Using single cell RNA sequencing approaches, we sequenced more than 100'000 cells and
576 generated a comprehensive dataset of the muscle microenvironment of patients with PAD as well as
577 healthy controls (undergoing angioplasty for an aneurysm). We chose to go for a single cell, and not
578 single nuclear approach, because of our specific interest in characterizing the muscle
579 microenvironment in PAD. Using this approach, 90% of the high-quality cells were mononuclear cells,
580 which allowed us to map the composition and transcriptional signature of the muscle
581 microenvironment in PAD with unprecedented detail. Our dataset provides a toolbox for the
582 community that allows to investigate the transcriptomic alterations in the PAD microenvironment in a
583 cell-type dependent fashion. All data are available at GSE235143. Within this manuscript, we chose to
584 focus on endothelial cells (ECs) and macrophages.

585 We identified common EC subpopulations such as arterial, venous, capillary and even
586 lymphatic populations which we were able to annotate using previously published markers[31,67]. We
587 also found two subpopulations of venous and capillary ECs in human skeletal muscle that are
588 characterized by high levels and activity of the transcription factors ATF3/4. The presence of the
589 ATF3/4$^+$ subset confirmed earlier work in mouse models which showed that ATF3/4$^+$ ECs have a higher
590 angiogenic capacity when compared to ATF3/4$^-$ ECs and are metabolically prepared for angiogenesis.
591 As a consequence, removing ATF4 from ECs prevented exercise-induced angiogenesis[31]. Similarly,
592 deletion of ATF3 reduced endothelial proliferation and impaired aorta regeneration[71], suggesting that
593 ATF3/4$^+$ ECs have distinct and specific characteristics. Our scRNAseq data further showed that the
594 fraction of ATF3/4$^+$ ECs was lower in PAD. Also, these ECs changed their ATF3/4 transcriptomic
595 signature and downregulated angiogenic as well as immune regulatory pathways, suggesting that the
596 immune regulatory role of ECs gets (at least partially) lost during PAD.

597 We measured an almost 3-fold rise in the number of CD68$^+$ cells on tissue sections.
598 Interestingly, most of those were *LYVE1*$^+$ resident macrophages and not recruited monocyte-derived
599 macrophages. In fact, while the fraction of monocytes went up in PAD, this did not translate into
600 increased monocyte-derived macrophage number and suggests impaired differentiation of recruited
601 macrophages. Preclinical mouse models for muscle ischemia have unequivocally supported the
602 requirement of recruited monocyte-derived macrophages for muscle regeneration. Injections of
603 clodronate loaded liposomes[120] or genetic depletion of CCR2[121] and other strategies that prevent
604 monocyte-derived macrophage accumulation, impair revascularization, regeneration, and/or
605 reperfusion of the ischemic limb. It is unclear whether the failed accumulation of monocyte-derived
606 macrophages is a result of the chronic nature of PAD or contributing to the impaired regenerative
607 response.

608 The majority of the muscle macrophage population, even under a setting of chronic
609 inflammation such as PAD, were LYVE1^{hi}MHCII^{low} macrophages. LYVE1^{hi}MHCII^{low} macrophages are
610 localized close to blood vessels (perivascular macrophages) in most tissues and have a distinct gene
611 expression profile, phenotype and function compared to monocyte-derived macrophages[100,122,123].
612 Single cell analysis in murine skeletal muscle previously identified the presence of Lyve1^{low}MHCII^{hi} and
613 Lyve1^{hi}MHCII^{low} subpopulations in the muscle[101]. Interestingly, Lyve1^{hi}MHCII^{low} macrophages are
614 embryonically derived, proliferate locally and self-renew with minimal monocyte input, showing that
615 they are resident muscle macrophages[94]. The role (and even composition) of the resident macrophage
616 population(s) in muscle is still poorly understood. They cloak microlesions to prevent widespread
617 neutrophil recruitment[124]. Upon acute damage, they crucially contribute to the clearance of damage-
618 induced apoptotic cells[96], but there is no evidence that they actively contribute to PAD muscle
619 pathology. Resident macrophages express FOLR2 and other markers which are typically associated
620 with M2-like regenerative macrophages such as CD163 and MRC1 (CD206), but we found that during
621 PAD, they also activate a pro-inflammatory gene program. The co-expression of genes that are typically
622 associated with an M1 as well as M2-like state, might potentially explain the contrasting findings that
623 have been reported in literature[29,30]. Recently, TIMD4 was proposed as a marker to isolate resident
624 macrophages from mouse muscle[96], but we could not detect *TIMD4* expression in human
625 macrophages. Whether and how resident macrophages contribute to skeletal muscle pathology in PAD
626 remains to be investigated. Previous work has however linked resident macrophages with vascular
627 permeability and increased vessel density in non-muscle tissues, though also non-resident
628 macrophages were depleted in those studies[95,125]. Also, perivascular resident skin macrophages
629 protrude into the vascular lumen and are skewed towards an anti-inflammatory phenotype while
630 insensitive to pro-inflammatory stimuli and play distinct roles in skin regeneration when compared to
631 recruited monocyte-derived-macrophages[126]. In the lung, depletion of LYVE1^{hi} macrophages leads to
632 vessel leakiness and fibrosis, suggesting widespread activation of fibroblasts[100]. Future research needs
633 to unravel whether the reduced (and altered) crosstalk between ECs and perivascular macrophages
634 contributes to PAD muscle pathology.

635 In depth analysis of the transcriptomic changes in microvascular capillary ECs revealed that
636 PAD is associated with a partial EndoMT signature. EndoMT has already been observed in coronary
637 artery ECs from patients with atherosclerosis[127]. Also, a fraction of arterioles of patients with CLI
638 undergo partial EndoMT and retain endothelial markers while activating SMAD2/3 signaling[12]. It has
639 been reported before that ischemia promotes the activation of EndoMT in clonally expanding ECs in
640 several pathological settings[128]. Also, in myocardial infarction, partial activation of an EndoMT state is
641 required for optimal angiogenesis[83]. We did not observe any proliferating ECs in PAD patients (data
642 not shown). However, it is possible that prolonged states of hypoxia contributed to a state of partial,

643 and chronic EndoMT. While we did observe activation of some, but not all, markers of EndoMT in PAD
644 capillary ECs, genes involved in ECM were significantly activated. Also, the endothelial marker *CDH5*
645 was reduced, but not lost, in PAD. Interestingly, this state of partial EndoMT might be reversible[83].

646 Despite the pronounced increase in vascular density, all patients enrolled in the study reported
647 intermittent claudication during exercise (Fontaine IIb) or even under resting conditions (Fontaine III-
648 IV). Potentially, the presence of a thickened ECM and/or basement membrane might limit oxygen and
649 nutrient diffusion into the ischemic myofibers. In fact, increased thickness of Collagen IV^+ basement
650 membrane was already shown in PAD[13]. Also, as part of the EndoMT signature, ECs in PAD
651 downregulated genes involved in lipid transport and trafficking. Beyond reducing endothelial lipid
652 metabolism, this might affect lipid transport since loss of FABP4 in ECs has been shown to reduce lipid
653 transport into lipid consuming muscles[129]. It will be exciting to investigate whether reversing EndoMT
654 in PAD patients could affect capillary ECs properties and restore oxygen and nutrient delivery to the
655 muscle.

656 Monocyte-derived macrophages contribute to arteriogenesis as well as
657 angiogenesis[11,23,26,29,65,85] and control perfusion upon hindlimb ischemia[27]. On the other hand,
658 endothelial cells also control macrophage differentiation[130], and fate specification via direct contact[131]
659 or via the secretion of angiocrine factors[27]. We detected strong cellular crosstalk between different
660 cell types in the muscle microenvironment that was significantly altered in PAD. Interestingly, FAPs
661 turned out to be main players controlling muscle homeostasis, but how FAPs contribute to the muscle
662 pathology in PAD needs further investigation. We found that IL1B signaling was one of the top
663 activated pathways in PAD. IL1B is a known regulator of EndoMT[132]. But also, a study using
664 canakinumab, an IL1B blocker, improved maximum and pain-free walking distance in patients with
665 symptomatic PAD while it failed to reach its primary endpoint being an effect on plaque progression
666 in the superficial femoral artery[133]. Unfortunately, muscle pathology was not further investigated in
667 this study. Finally, we found that the activation of $LYVE1^{hi}MHCII^{low}$ resident macrophages could be
668 driven by ECs. Beyond having a perivascular localization, these data imply that ECs might control the
669 fate of resident macrophages, an exciting hypothesis that requires further investigation.

670 In conclusion, the contribution of skeletal muscle pathology to PAD progression is poorly
671 understood. We have used a single cell approach to characterize the composition and transcriptional
672 changes of the skeletal muscle microenvironment during PAD. We identify profound transcriptomic
673 alterations in endothelial cells and found that resident macrophages are the main macrophage
674 population in PAD muscle. Our dataset provides unprecedented insight into the skeletal muscle
675 microenvironment during PAD. We propose that unravelling the (impaired) cellular crosstalk in PAD
676 muscle could potentially offer novel targets for therapeutic intervention.

Acknowledgments

The authors thank the digital trial intervention platform (dTIP) from ETH Zurich for their skilled assistance and the Functional Genomics Center Zürich (FGCZ) for excellent technical support.

Sources of funding

This project was funded by a Swiss National Science Foundation (SNSF) project grant (310030_208041). KDB is endowed by the Schulthess Foundation.

Disclosures

None.

Supplemental Material

Figures S1-S3

Supplemental File 1

688 ## References

689 1. Fowkes FGR, Aboyans V, Fowkes FJI, McDermott MM, Sampson UKA, Criqui MH. Peripheral
690 artery disease: epidemiology and global perspectives. *Nat Rev Cardiol*. 2017;14:156–170.

691 2. Fowkes FGR, Rudan D, Rudan I, Aboyans V, Denenberg JO, McDermott MM, Norman PE,
692 Sampson UKA, Williams LJ, Mensah GA, et al. Comparison of global estimates of prevalence
693 and risk factors for peripheral artery disease in 2000 and 2010: a systematic review and
694 analysis. *Lancet*. 2013;382:1329–40.

695 3. De Stefano F, Rios LHP, Fiani B, Fareed J, Tafur A. National Trends for Peripheral Artery
696 Disease and End Stage Renal Disease From the National Inpatient Sample Database. *Clin Appl*
697 *Thromb Hemost*. 2021;27:10760296211025624.

698 4. ROSE GA. The diagnosis of ischaemic heart pain and intermittent claudication in field surveys.
699 *Bull World Health Organ*. 1962;27:645–58.

700 5. Bethel M, Annex BH. Peripheral arterial disease: A small and large vessel problem. *American*
701 *Heart Journal Plus: Cardiology Research and Practice*. 2023;28:100291.

702 6. Cooke JP, Meng S. Vascular Regeneration in Peripheral Artery Disease. *Arterioscler Thromb*
703 *Vasc Biol*. 2020;40:1627–1634.

704 7. Annex BH. Therapeutic angiogenesis for critical limb ischaemia. *Nat Rev Cardiol*. 2013;10:387–
705 396.

706 8. West AM, Anderson JD, Epstein FH, Meyer CH, Hagspiel KD, Berr SS, Harthun NL, Weltman AL,
707 Annex BH, Kramer CM. Percutaneous intervention in peripheral artery disease improves calf
708 muscle phosphocreatine recovery kinetics: A pilot study. *Vascular Medicine*. 2012;17:3–9.

709 9. Kodama A, Takahara M, Iida O, Soga Y, Terashi H, Kawasaki D, Izumi Y, Mii S, Komori K, Azuma
710 N. Ambulatory Status Over Time after Revascularization in Patients with Chronic Limb-
711 Threatening Ischemia. *J Atheroscler Thromb*. 2022;29:62892.

712 10. Gianni-Barrera R, Bartolomeo M, Vollmar B, Djonov V, Banfi A. Split for the cure: VEGF, PDGF-
713 BB and intussusception in therapeutic angiogenesis. *Biochem Soc Trans*. 2014;42:1637–42.

714 11. Simons M, Ware JA. Therapeutic angiogenesis in cardiovascular disease. *Nat Rev Drug Discov*.
715 2003;2:863–71.

716 12. Chevalier J, Yin H, Arpino J-M, O'Neil C, Nong Z, Gilmore KJ, Lee JJ, Prescott E, Hewak M, Rice
717 CL, et al. Obstruction of Small Arterioles in Patients with Critical Limb Ischemia due to Partial
718 Endothelial-to-Mesenchymal Transition. *iScience*. 2020;23:101251.

719 13. Mietus CJ, Lackner TJ, Karvelis PS, Willcockson GT, Shields CM, Lambert NG, Koutakis P,
720 Fuglestad MA, Hernandez H, Haynatzki GR, et al. Abnormal Microvascular Architecture,
721 Fibrosis, and Pericyte Characteristics in the Calf Muscle of Peripheral Artery Disease Patients
722 with Claudication and Critical Limb Ischemia. *J Clin Med*. 2020;9:2575.

723 14. Coats P, Hillier C. Differential Responses in Human Subcutaneous and Skeletal Muscle Vascular
724 Beds to Critical Limb Ischaemia. *European Journal of Vascular and Endovascular Surgery*.
725 2000;19:387–395.

726 15. Hammarsten J, Bylund-Fellenius AC, Holm J, Scherstén T, Krotkiewski M. Capillary supply and
727 muscle fibre types in patients with intermittent claudication: relationships between
728 morphology and metabolism. *Eur J Clin Invest*. 1980;10:301–5.

729 16. Ho TK, Rajkumar V, Ponticos M, Leoni P, Black DCM, Abraham DJ, Baker DM. Increased
730 endogenous angiogenic response and hypoxia-inducible factor-1α in human critical limb
731 ischemia. *J Vasc Surg*. 2006;43:125–133.

732 17. McGuigan MR, Bronks R, Newton RU, Sharman MJ, Graham JC, Cody D V, Kraemer WJ. Muscle
733 fiber characteristics in patients with peripheral arterial disease. *Med Sci Sports Exerc*.
734 2001;33:2016–21.

735 18. Tsui JCS, Baker DM, Biecker E, Shaw S, Dashwood MR. Potential role of endothelin 1 in
736 ischaemia-induced angiogenesis in critical leg ischaemia. *Br J Surg*. 2002;89:741–7.

737 19. Clyne CA, Mears H, Weller RO, O'Donnell TF. Calf muscle adaptation to peripheral vascular
738 disease. *Cardiovasc Res*. 1985;19:507–12.

739 20. Robbins JL, Jones WS, Duscha BD, Allen JD, Kraus WE, Regensteiner JG, Hiatt WR, Annex BH.
740 Relationship between leg muscle capillary density and peak hyperemic blood flow with
741 endurance capacity in peripheral artery disease. *J Appl Physiol (1985)*. 2011;111:81–6.

742 21. Christov C, Chrétien F, Abou-Khalil R, Bassez G, Vallet G, Authier F-J, Bassaglia Y, Shinin V,
743 Tajbakhsh S, Chazaud B, et al. Muscle satellite cells and endothelial cells: close neighbors and
744 privileged partners. *Mol Biol Cell*. 2007;18:1397–409.

745 22. Méndez-Barbero N, Gutiérrez-Muñoz C, Blanco-Colio L. Cellular Crosstalk between Endothelial
746 and Smooth Muscle Cells in Vascular Wall Remodeling. *Int J Mol Sci*. 2021;22:7284.

747 23. Krishnasamy K, Limbourg A, Kapanadze T, Gamrekelashvili J, Beger C, Häger C, Lozanovski VJ,
748 Falk CS, Napp LC, Bauersachs J, et al. Blood vessel control of macrophage maturation
749 promotes arteriogenesis in ischemia. *Nat Commun*. 2017;8:952.

750 24. Amersfoort J, Eelen G, Carmeliet P. Immunomodulation by endothelial cells — partnering up
751 with the immune system? *Nat Rev Immunol*. 2022;22:576–588.

752 25. Dort J, Fabre P, Molina T, Dumont NA. Macrophages Are Key Regulators of Stem Cells during
753 Skeletal Muscle Regeneration and Diseases. *Stem Cells Int*. 2019;2019:4761427.

754 26. Ganta VC, Choi MH, Kutateladze A, Fox TE, Farber CR, Annex BH. A MicroRNA93–Interferon
755 Regulatory Factor-9–Immunoresponsive Gene-1–Itaconic Acid Pathway Modulates M2-Like
756 Macrophage Polarization to Revascularize Ischemic Muscle. *Circulation*. 2017;135:2403–2425.

757 27. Zhang J, Muri J, Fitzgerald G, Gorski T, Gianni-Barrera R, Masschelein E, D'Hulst G, Gilardoni P,
758 Turiel G, Fan Z, et al. Endothelial Lactate Controls Muscle Regeneration from Ischemia by
759 Inducing M2-like Macrophage Polarization. *Cell Metab*. 2020;31:1136-1153.e7.

760 28. Casale GP, Thompson JR, Carpenter LC, Kim J, Lackner TJ, Mietus CJ, Ha DM, Myers SA,
761 Brunette KE, Li S, et al. Cytokine signature of inflammation mediated by autoreactive Th-cells,
762 in calf muscle of claudicating patients with Fontaine stage II peripheral artery disease.
763 *Translational Research*. 2021;228:94–108.

764 29. Ganta VC, Choi M, Farber CR, Annex BH. Antiangiogenic VEGF $_{165}$ b Regulates Macrophage
765 Polarization via S100A8/S100A9 in Peripheral Artery Disease. *Circulation*. 2019;139:226–242.

766 30. Kosmac K, Gonzalez-Freire M, McDermott MM, White SH, Walton RG, Sufit RL, Tian L, Li L,
767 Kibbe MR, Criqui MH, et al. Correlations of Calf Muscle Macrophage Content With Muscle
768 Properties and Walking Performance in Peripheral Artery Disease. *J Am Heart Assoc*. 2020;9.

769 31. Fan Z, Turiel G, Ardicoglu R, Ghobrial M, Masschelein E, Kocijan T, Zhang J, Tan G, Fitzgerald G,
770 Gorski T, et al. Exercise-induced angiogenesis is dependent on metabolically primed ATF3/4+
771 endothelial cells. *Cell Metab*. 2021;33:1793-1807.e9.

772 32. Brevetti G, Giugliano G, Brevetti L, Hiatt WR. Inflammation in Peripheral Artery Disease.
773 *Circulation*. 2010;122:1862–1875.

774 33. Silvestro A, Scopacasa F, Ruocco A, Oliva G, Schiano V, Zincarelli C, Brevetti G. Inflammatory
775 status and endothelial function in asymptomatic and symptomatic peripheral arterial disease.
776 *Vasc Med*. 2003;8:225–32.

777 34. McDermott MM, Guralnik JM, Corsi A, Albay M, Macchi C, Bandinelli S, Ferrucci L. Patterns of
778 inflammation associated with peripheral arterial disease: the InCHIANTI study. *Am Heart J*.
779 2005;150:276–81.

780 35. Madissoon E, Wilbrey-Clark A, Miragaia RJ, Saeb-Parsy K, Mahbubani KT, Georgakopoulos N,
781 Harding P, Polanski K, Huang N, Nowicki-Osuch K, et al. scRNA-seq assessment of the human
782 lung, spleen, and esophagus tissue stability after cold preservation. *Genome Biol*. 2020;21:1.

783 36. Lun ATL, McCarthy DJ, Marioni JC. A step-by-step workflow for low-level analysis of single-cell
784 RNA-seq data with Bioconductor. *F1000Res* [Internet]. 2016;5:2122. Available from:
785 https://f1000research.com/articles/5-2122/v2

786 37. McCarthy DJ, Campbell KR, Lun ATL, Wills QF. Scater: Pre-processing, quality control,
787 normalization and visualization of single-cell RNA-seq data in R. *Bioinformatics*.
788 2017;33:1179–1186.

789 38. Hong R, Koga Y, Bandyadka S, Leshchyk A, Wang Y, Akavoor V, Cao X, Sarfraz I, Wang Z,
790 Alabdullatif S, et al. Comprehensive generation, visualization, and reporting of quality control
791 metrics for single-cell RNA sequencing data. *Nat Commun*. 2022;13:1688.

792 39. Korsunsky I, Millard N, Fan J, Slowikowski K, Zhang F, Wei K, Baglaenko Y, Brenner M, Loh P,
793 Raychaudhuri S. Fast, sensitive and accurate integration of single-cell data with Harmony. *Nat*
794 *Methods*. 2019;16:1289–1296.

795 40. Hao Y, Hao S, Andersen-Nissen E, Mauck WM, Zheng S, Butler A, Lee MJ, Wilk AJ, Darby C,
796 Zager M, et al. Integrated analysis of multimodal single-cell data. *Cell*. 2021;184:3573-
797 3587.e29.

798 41. Raudvere U, Kolberg L, Kuzmin I, Arak T, Adler P, Peterson H, Vilo J. g:Profiler: a web server for
799 functional enrichment analysis and conversions of gene lists (2019 update). *Nucleic Acids Res*.
800 2019;47:W191–W198.

801 42. Sayols S. rrvgo: a Bioconductor package for interpreting lists of Gene Ontology terms.
802 *MicroPubl Biol*. 2023;2023.

803 43. Luo W, Brouwer C. Pathview: an R/Bioconductor package for pathway-based data integration
804 and visualization. *Bioinformatics*. 2013;29:1830–1.

805 44. Love MI, Huber W, Anders S. Moderated estimation of fold change and dispersion for RNA-seq
806 data with DESeq2. *Genome Biol*. 2014;15:550.

807 45. Korotkevich G, Sukhov V, Budin N, Shpak B, Artyomov MN, Sergushichev A. Fast gene set
808 enrichment analysis. *bioRxiv* [Internet]. 2021;060012. Available from:
809 http://biorxiv.org/content/early/2021/02/01/060012.abstract

810 46. Liberzon A, Birger C, Thorvaldsdóttir H, Ghandi M, Mesirov JP, Tamayo P. The Molecular
811 Signatures Database Hallmark Gene Set Collection. *Cell Syst*. 2015;1:417–425.

812 47. Hänzelmann S, Castelo R, Guinney J. GSVA: gene set variation analysis for microarray and
813 RNA-seq data. *BMC Bioinformatics*. 2013;14:7.

814 48. Sanin DE, Ge Y, Marinkovic E, Kabat AM, Castoldi A, Caputa G, Grzes KM, Curtis JD, Thompson
815 EA, Willenborg S, et al. A common framework of monocyte-derived macrophage activation.
816 *Sci Immunol*. 2022;7.

817 49. Varga T, Mounier R, Horvath A, Cuvellier S, Dumont F, Poliska S, Ardjoune H, Juban G, Nagy L,
818 Chazaud B. Highly Dynamic Transcriptional Signature of Distinct Macrophage Subsets during
819 Sterile Inflammation, Resolution, and Tissue Repair. *The Journal of Immunology*.
820 2016;196:4771–4782.

821 50. Aibar S, González-Blas CB, Moerman T, Huynh-Thu VA, Imrichova H, Hulselmans G, Rambow F,
822 Marine J-C, Geurts P, Aerts J, et al. SCENIC: single-cell regulatory network inference and
823 clustering. *Nat Methods*. 2017;14:1083–1086.

824 51. González-Blas CB, De Winter S, Hulselmans G, Hecker N, Matetovici I, Christiaens V,
825 Poovathingal S, Wouters J, Aibar S, Aerts S. SCENIC+: single-cell multiomic inference of
826 enhancers and gene regulatory networks. *bioRxiv* [Internet]. 2022;2022.08.19.504505.
827 Available from: http://biorxiv.org/content/early/2022/08/19/2022.08.19.504505.abstract

828 52. Jin S, Guerrero-Juarez CF, Zhang L, Chang I, Ramos R, Kuan C-H, Myung P, Plikus M V., Nie Q.
829 Inference and analysis of cell-cell communication using CellChat. *Nat Commun*. 2021;12:1088.

830 53. Browaeys R, Saelens W, Saeys Y. NicheNet: modeling intercellular communication by linking
831 ligands to target genes. *Nat Methods*. 2020;17:159–162.

832 54. Jones RC, Karkanias J, Krasnow MA, Pisco AO, Quake SR, Salzman J, Yosef N, Bulthaup B,
833 Brown P, Harper W, et al. The Tabula Sapiens: A multiple-organ, single-cell transcriptomic
834 atlas of humans. *Science (1979)*. 2022;376.

835 55. de Micheli AJ, Spector JA, Elemento O, Cosgrove BD. A reference single-cell transcriptomic
836 atlas of human skeletal muscle tissue reveals bifurcated muscle stem cell populations. *Skelet*
837 *Muscle*. 2020;10:19.

838 56. Rubenstein AB, Smith GR, Raue U, Begue G, Minchev K, Ruf-Zamojski F, Nair VD, Wang X, Zhou
839 L, Zaslavsky E, et al. Single-cell transcriptional profiles in human skeletal muscle. *Sci Rep*.
840 2020;10:1–15.

841 57. Cameron A, Wakelin G, Gaulton N, Young L V., Wotherspoon S, Hodson N, Lees MJ, Moore DR,
842 Johnston AP. Identification of underexplored mesenchymal and vascular-related cell
843 populations in human skeletal muscle. *American Journal of Physiology-Cell Physiology*.
844 2022;323:C1586–C1600.

845 58. De Micheli AJ, Laurilliard EJ, Heinke CL, Ravichandran H, Fraczek P, Soueid-Baumgarten S, De
846 Vlaminck I, Elemento O, Cosgrove BD. Single-Cell Analysis of the Muscle Stem Cell Hierarchy

847 Identifies Heterotypic Communication Signals Involved in Skeletal Muscle Regeneration. *Cell*
848 *Rep*. 2020;30:3583-3595.e5.

849 59. Love MI, Huber W, Anders S. Moderated estimation of fold change and dispersion for RNA-seq
850 data with DESeq2. *Genome Biol*. 2014;15:550.

851 60. Pande RL, Brown J, Buck S, Redline W, Doyle J, Plutzky J, Creager MA. Association of monocyte
852 tumor necrosis factor α expression and serum inflammatory biomarkers with walking
853 impairment in peripheral artery disease. *J Vasc Surg*. 2015;61:155–61.

854 61. Signorelli SS, Mazzarino MC, Di Pino L, Malaponte G, Porto C, Pennisi G, Marchese G, Costa
855 MP, Digrandi D, Celotta G, et al. High circulating levels of cytokines (IL-6 and TNFalpha),
856 adhesion molecules (VCAM-1 and ICAM-1) and selectins in patients with peripheral arterial
857 disease at rest and after a treadmill test. *Vasc Med*. 2003;8:15–9.

858 62. Ferrucci L, Candia J, Ubaida-Mohien C, Lyaskov A, Banskota N, Leeuwenburgh C, Wohlgemuth
859 S, Guralnik JM, Kaileh M, Zhang D, et al. Transcriptomic and Proteomic of Gastrocnemius
860 Muscle in Peripheral Artery Disease. *Circ Res*. 2023;

861 63. Ryan TE, Yamaguchi DJ, Schmidt CA, Zeczycki TN, Shaikh SR, Brophy P, Green TD, Tarpey MD,
862 Karnekar R, Goldberg EJ, et al. Extensive skeletal muscle cell mitochondriopathy distinguishes
863 critical limb ischemia patients from claudicants. *JCI Insight*. 2018;3.

864 64. Santos M Dos, Gioftsidi S, Backer S, Machado L, Relaix F, Maire P, Mourikis P. Extraction and
865 sequencing of single nuclei from murine skeletal muscles. *STAR Protoc*. 2021;2:100694.

866 65. Tan RP, Ryder I, Yang N, Lam YT, Santos M, Michael PL, Robinson DA, Ng MK, Wise SG.
867 Macrophage Polarization as a Novel Therapeutic Target for Endovascular Intervention in
868 Peripheral Artery Disease. *JACC Basic Transl Sci*. 2021;6:693–704.

869 66. Kavurma MM, Bursill C, Stanley CP, Passam F, Cartland SP, Patel S, Loa J, Figtree GA, Golledge
870 J, Aitken S, et al. Endothelial cell dysfunction: Implications for the pathogenesis of peripheral
871 artery disease. *Front Cardiovasc Med*. 2022;9:1054576.

872 67. Kalucka J, de Rooij LPMH, Goveia J, Rohlenova K, Dumas SJ, Meta E, Conchinha N V, Taverna F,
873 Teuwen L-A, Veys K, et al. Single-Cell Transcriptome Atlas of Murine Endothelial Cells. *Cell*.
874 2020;180:764-779.e20.

875 68. Kanehisa M, Sato Y, Kawashima M, Furumichi M, Tanabe M. KEGG as a reference resource for
876 gene and protein annotation. *Nucleic Acids Res*. 2016;44:D457–D462.

877 69. Wedgwood JF, Hatam L, Bonagura VR. Effect of interferon-gamma and tumor necrosis factor
878 on the expression of class I and class II major histocompatibility molecules by cultured human
879 umbilical vein endothelial cells. *Cell Immunol*. 1988;111:1–9.

880 70. Mai J, Nanayakkara G, Lopez-Pastrana J, Li X, Li Y-F, Wang X, Song A, Virtue A, Shao Y, Shan H,
881 et al. Interleukin-17A Promotes Aortic Endothelial Cell Activation via Transcriptionally and
882 Post-translationally Activating p38 Mitogen-activated Protein Kinase (MAPK) Pathway. *J Biol*
883 *Chem*. 2016;291:4939–54.

884 71. McDonald AI, Shirali AS, Aragón R, Ma F, Hernandez G, Vaughn DA, Mack JJ, Lim TY, Sunshine
885 H, Zhao P, et al. Endothelial Regeneration of Large Vessels Is a Biphasic Process Driven by
886 Local Cells with Distinct Proliferative Capacities. *Cell Stem Cell*. 2018;23:210-225.e6.

887 72. Hänzelmann S, Castelo R, Guinney J. GSVA: gene set variation analysis for microarray and
888 RNA-Seq data. *BMC Bioinformatics*. 2013;14:7.

889 73. Ashburner M, Ball CA, Blake JA, Botstein D, Butler H, Cherry JM, Davis AP, Dolinski K, Dwight
890 SS, Eppig JT, et al. Gene ontology: tool for the unification of biology. The Gene Ontology
891 Consortium. *Nat Genet*. 2000;25:25–9.

892 74. Gene Ontology Consortium. The Gene Ontology resource: enriching a GOld mine. *Nucleic*
893 *Acids Res*. 2021;49:D325–D334.

894 75. Tellez-Plaza M, Guallar E, Fabsitz RR, Howard B V, Umans JG, Francesconi KA, Goessler W,
895 Devereux RB, Navas-Acien A. Cadmium exposure and incident peripheral arterial disease. *Circ*
896 *Cardiovasc Qual Outcomes*. 2013;6:626–33.

897 76. Tinkov AA, Filippini T, Ajsuvakova OP, Skalnaya MG, Aaseth J, Bjørklund G, Gatiatulina ER,
898 Popova E V, Nemereshina ON, Huang P-T, et al. Cadmium and atherosclerosis: A review of
899 toxicological mechanisms and a meta-analysis of epidemiologic studies. *Environ Res*.
900 2018;162:240–260.

901 77. Stadler N, Stanley N, Heeneman S, Vacata V, Daemen MJAP, Bannon PG, Waltenberger J,
902 Davies MJ. Accumulation of Zinc in Human Atherosclerotic Lesions Correlates With Calcium
903 Levels But Does Not Protect Against Protein Oxidation. *Arterioscler Thromb Vasc Biol*.
904 2008;28:1024–1030.

905 78. Bagheri B, Akbari N, Tabiban S, Habibi V, Mokhberi V. Serum level of copper in patients with
906 coronary artery disease. *Niger Med J*. 2015;56:39–42.

907 79. Navas-Acien A, Silbergeld EK, Sharrett R, Calderon-Aranda E, Selvin E, Guallar E. Metals in
908 urine and peripheral arterial disease. *Environ Health Perspect*. 2005;113:164–9.

909 80. Knoflach M, Messner B, Shen YH, Frotschnig S, Liu G, Pfaller K, Wang X, Matosevic B, Willeit J,
910 Kiechl S, et al. Non-toxic cadmium concentrations induce vascular inflammation and promote
911 atherosclerosis. *Circ J*. 2011;75:2491–5.

912 81. Liang H, Yue R, Zhou C, Liu M, Yu X, Lu S, Zeng J, Yu Z, Zhou Z, Hu H. Cadmium exposure
913 induces endothelial dysfunction via disturbing lipid metabolism in human microvascular
914 endothelial cells. *J Appl Toxicol*. 2021;41:775–788.

915 82. Yeh S-C, Tsai F-Y, Chao H-R, Tsou T-C. Zinc ions induce inflammatory responses in vascular
916 endothelial cells. *Bull Environ Contam Toxicol*. 2011;87:113–6.

917 83. Tombor LS, John D, Glaser SF, Luxán G, Forte E, Furtado M, Rosenthal N, Baumgarten N,
918 Schulz MH, Wittig J, et al. Single cell sequencing reveals endothelial plasticity with transient
919 mesenchymal activation after myocardial infarction. *Nat Commun*. 2021;12:681.

920 84. Hynes RO, Naba A. Overview of the matrisome--an inventory of extracellular matrix
921 constituents and functions. *Cold Spring Harb Perspect Biol*. 2012;4:a004903.

922 85. Hamm A, Veschini L, Takeda Y, Costa S, Delamarre E, Squadrito ML, Henze A, Wenes M,
923 Serneels J, Pucci F, et al. PHD2 regulates arteriogenic macrophages through TIE2 signalling.
924 *EMBO Mol Med*. 2013;5:843–857.

925 86. Mosser DM, Edwards JP. Exploring the full spectrum of macrophage activation. *Nat Rev*
926 *Immunol*. 2008;8:958–69.

927 87. Arnold L, Henry A, Poron F, Baba-Amer Y, van Rooijen N, Plonquet A, Gherardi RK, Chazaud B.
928 Inflammatory monocytes recruited after skeletal muscle injury switch into antiinflammatory
929 macrophages to support myogenesis. *J Exp Med*. 2007;204:1057–69.

930 88. Raes G, De Baetselier P, Noël W, Beschin A, Brombacher F, Hassanzadeh Gh G. Differential
931 expression of FIZZ1 and Ym1 in alternatively versus classically activated macrophages. *J*
932 *Leukoc Biol*. 2002;71:597–602.

933 89. Deng B, Wehling-Henricks M, Villalta SA, Wang Y, Tidball JG. IL-10 triggers changes in
934 macrophage phenotype that promote muscle growth and regeneration. *J Immunol*.
935 2012;189:3669–80.

936 90. Tidball JG, Wehling-Henricks M. Macrophages promote muscle membrane repair and muscle
937 fibre growth and regeneration during modified muscle loading in mice in vivo. *J Physiol*.
938 2007;578:327–36.

939 91. Ochoa O, Sun D, Reyes-Reyna SM, Waite LL, Michalek JE, McManus LM, Shireman PK. Delayed
940 angiogenesis and VEGF production in CCR2-/- mice during impaired skeletal muscle
941 regeneration. *Am J Physiol Regul Integr Comp Physiol*. 2007;293:R651-61.

942 92. Zhu H, Zhang M, Liu Z, Xing J, Moriasi C, Dai X, Zou M-H. AMP-Activated Protein Kinase α1 in
943 Macrophages Promotes Collateral Remodeling and Arteriogenesis in Mice In Vivo. *Arterioscler*
944 *Thromb Vasc Biol*. 2016;36:1868–78.

945 93. Mulder K, Patel AA, Kong WT, Piot C, Halitzki E, Dunsmore G, Khalilnezhad S, Irac SE,
946 Dubuisson A, Chevrier M, et al. Cross-tissue single-cell landscape of human monocytes and
947 macrophages in health and disease. *Immunity*. 2021;54:1883-1900.e5.

948 94. Dick SA, Wong A, Hamidzada H, Nejat S, Nechanitzky R, Vohra S, Mueller B, Zaman R, Kantores
949 C, Aronoff L, et al. Three tissue resident macrophage subsets coexist across organs with
950 conserved origins and life cycles. *Sci Immunol*. 2022;7.

951 95. Moura Silva H, Kitoko JZ, Queiroz CP, Kroehling L, Matheis F, Yang KL, Reis BS, Ren-Fielding C,
952 Littman DR, Bozza MT, et al. c-MAF–dependent perivascular macrophages regulate diet-
953 induced metabolic syndrome. *Sci Immunol*. 2021;6.

954 96. Babaeijandaghi F, Cheng R, Kajabadi N, Soliman H, Chang C-K, Smandych J, Tung LW, Long R,
955 Ghassemi A, Rossi FM V. Metabolic reprogramming of skeletal muscle by resident
956 macrophages points to CSF1R inhibitors as muscular dystrophy therapeutics. *Sci Transl Med*.
957 2022;14.

958 97. Ziegler-Heitbrock L, Ancuta P, Crowe S, Dalod M, Grau V, Hart DN, Leenen PJM, Liu Y-J,
959 MacPherson G, Randolph GJ, et al. Nomenclature of monocytes and dendritic cells in blood.
960 *Blood*. 2010;116:e74-80.

961 98. Geissmann F, Jung S, Littman DR. Blood Monocytes Consist of Two Principal Subsets with
962 Distinct Migratory Properties. *Immunity*. 2003;19:71–82.

963 99. Auffray C, Fogg D, Garfa M, Elain G, Join-Lambert O, Kayal S, Sarnacki S, Cumano A, Lauvau G,
964 Geissmann F. Monitoring of Blood Vessels and Tissues by a Population of Monocytes with
965 Patrolling Behavior. *Science (1979)*. 2007;317:666–670.

966 100. Chakarov S, Lim HY, Tan L, Lim SY, See P, Lum J, Zhang X-M, Foo S, Nakamizo S, Duan K, et al.
967 Two distinct interstitial macrophage populations coexist across tissues in specific subtissular
968 niches. *Science (1979)*. 2019;363.

969 101. Wang X, Sathe AA, Smith GR, Ruf-Zamojski F, Nair V, Lavine KJ, Xing C, Sealfon SC, Zhou L.
970 Heterogeneous origins and functions of mouse skeletal muscle-resident macrophages.
971 *Proceedings of the National Academy of Sciences*. 2020;117:20729–20740.

972 102. Lin J-D, Nishi H, Poles J, Niu X, Mccauley C, Rahman K, Brown EJ, Yeung ST, Vozhilla N,
973 Weinstock A, et al. Single-cell analysis of fate-mapped macrophages reveals heterogeneity,
974 including stem-like properties, during atherosclerosis progression and regression. *JCI Insight*.
975 2019;4.

976 103. Martinez FO, Gordon S. The M1 and M2 paradigm of macrophage activation: time for
977 reassessment. *F1000Prime Rep*. 2014;6.

978 104. Mantovani , Alberto, Sica , Antonio, Locati M. Macrophage Polarization Comes of Age.
979 *Immunity*. 2005;23:344–346.

980 105. Palma A, Jarrah AS, Tieri P, Cesareni G, Castiglione F. Gene Regulatory Network Modeling of
981 Macrophage Differentiation Corroborates the Continuum Hypothesis of Polarization States.
982 *Front Physiol*. 2018;9:1659.

983 106. Orekhov AN, Nikiforov NG, Elizova N V, Korobov GA, Aladinskaya A V, Sobenin IA, Bobryshev Y
984 V. Tumor Necrosis Factor-α and C-C Motif Chemokine Ligand 18 Associate with
985 Atherosclerotic Lipid Accumulation In situ and In vitro. *Curr Pharm Des*. 2018;24:2883–2889.

986 107. Hägg DA, Olson FJ, Kjelldahl J, Jernås M, Thelle DS, Carlsson LMS, Fagerberg B, Svensson P-A.
987 Expression of chemokine (C-C motif) ligand 18 in human macrophages and atherosclerotic
988 plaques. *Atherosclerosis*. 2009;204:e15-20.

989 108. Halvorsen B, Espeland MZ, Andersen GØ, Yndestad A, Sagen EL, Rashidi A, Knudsen EC,
990 Skjelland M, Skagen KR, Krohg-Sørensen K, et al. Increased expression of NAMPT in PBMC
991 from patients with acute coronary syndrome and in inflammatory M1 macrophages.
992 *Atherosclerosis*. 2015;243:204–10.

993 109. de Jager SCA, Bongaerts BWC, Weber M, Kraaijeveld AO, Rousch M, Dimmeler S, van Dieijen-
994 Visser MP, Cleutjens KBJM, Nelemans PJ, van Berkel TJC, et al. Chemokines CCL3/MIP1α,
995 CCL5/RANTES and CCL18/PARC are independent risk predictors of short-term mortality in
996 patients with acute coronary syndromes. *PLoS One*. 2012;7:e45804.

997 110. Li S, Wang C, Li K, Li L, Tian M, Xie J, Yang M, Jia Y, He J, Gao L, et al. NAMPT knockdown
998 attenuates atherosclerosis and promotes reverse cholesterol transport in ApoE KO mice with
999 high-fat-induced insulin resistance. *Sci Rep*. 2016;6:26746.

1000 111. de Jager SCA, Bot I, Kraaijeveld AO, Korporaal SJA, Bot M, van Santbrink PJ, van Berkel TJC,
1001 Kuiper J, Biessen EAL. Leukocyte-Specific CCL3 Deficiency Inhibits Atherosclerotic Lesion
1002 Development by Affecting Neutrophil Accumulation. *Arterioscler Thromb Vasc Biol*. 2013;33.

1003 112. Brykczynska U, Geigges M, Wiedemann SJ, Dror E, Böni-Schnetzler M, Hess C, Donath MY,
1004 Paro R. Distinct Transcriptional Responses across Tissue-Resident Macrophages to Short-Term
1005 and Long-Term Metabolic Challenge. *Cell Rep*. 2020;30:1627-1643.e7.

1006 113. Dulin E, García-Barreno P, Guisasola MC. Genetic variations of HSPA1A, the heat shock protein
1007 levels, and risk of atherosclerosis. *Cell Stress Chaperones*. 2012;17:507–16.

1008 114. Sehgal A, Irvine KM, Hume DA. Functions of macrophage colony-stimulating factor (CSF1) in
1009 development, homeostasis, and tissue repair. *Semin Immunol*. 2021;54:101509.

1010 115. Sinha SK, Miikeda A, Fouladian Z, Mehrabian M, Edillor C, Shih D, Zhou Z, Paul MK,
1011 Charugundla S, Davis RC, et al. Local M-CSF (Macrophage Colony-Stimulating Factor)
1012 Expression Regulates Macrophage Proliferation and Apoptosis in Atherosclerosis. *Arterioscler*
1013 *Thromb Vasc Biol*. 2021;41:220–233.

1014 116. Deng T, Zhang Y, Chen Q, Yan K, Han D. Toll-like receptor-mediated inhibition of Gas6 and
1015 ProS expression facilitates inflammatory cytokine production in mouse macrophages.
1016 *Immunology*. 2012;135:40–50.

1017 117. Chiu K-C, Lee C-H, Liu S-Y, Chou Y-T, Huang R-Y, Huang S-M, Shieh Y-S. Polarization of tumor-
1018 associated macrophages and Gas6/Axl signaling in oral squamous cell carcinoma. *Oral Oncol*.
1019 2015;51:683–9.

1020 118. Fuster JJ, Walsh K. The Good, the Bad, and the Ugly of interleukin-6 signaling. *EMBO J*.
1021 2014;33:1425–1427.

1022 119. Fernando MR, Reyes JL, Iannuzzi J, Leung G, McKay DM. The pro-inflammatory cytokine,
1023 interleukin-6, enhances the polarization of alternatively activated macrophages. *PLoS One*.
1024 2014;9:e94188.

1025 120. Vågesjö E, Parv K, Ahl D, Seignez C, Herrera Hidalgo C, Giraud A, Leite C, Korsgren O, Wallén H,
1026 Juusola G, et al. Perivascular Macrophages Regulate Blood Flow Following Tissue Damage. *Circ*
1027 *Res*. 2021;128:1694–1707.

1028 121. Lu H, Huang D, Saederup N, Charo IF, Ransohoff RM, Zhou L. Macrophages recruited via CCR2
1029 produce insulin-like growth factor-1 to repair acute skeletal muscle injury. *FASEB J*.
1030 2011;25:358–69.

1031 122. Schyns J, Bai Q, Ruscitti C, Radermecker C, De Schepper S, Chakarov S, Farnir F, Pirottin D,
1032 Ginhoux F, Boeckxstaens G, et al. Non-classical tissue monocytes and two functionally distinct
1033 populations of interstitial macrophages populate the mouse lung. *Nat Commun*.
1034 2019;10:3964.

1035 123. Ural BB, Yeung ST, Damani-Yokota P, Devlin JC, de Vries M, Vera-Licona P, Samji T, Sawai CM,
1036 Jang G, Perez OA, et al. Identification of a nerve-associated, lung-resident interstitial
1037 macrophage subset with distinct localization and immunoregulatory properties. *Sci Immunol*.
1038 2020;5.

1039 124. Uderhardt S, Martins AJ, Tsang JS, Lämmermann T, Germain RN. Resident Macrophages Cloak
1040 Tissue Microlesions to Prevent Neutrophil-Driven Inflammatory Damage. *Cell*. 2019;177:541-
1041 555.e17.

1042 125. He H, Mack JJ, Güç E, Warren CM, Squadrito ML, Kilarski WW, Baer C, Freshman RD,
1043 McDonald AI, Ziyad S, et al. Perivascular Macrophages Limit Permeability. *Arterioscler Thromb*
1044 *Vasc Biol*. 2016;36:2203–2212.

1045 126. Barreiro O, Cibrian D, Clemente C, Alvarez D, Moreno V, Valiente Í, Bernad A, Vestweber D,
1046 Arroyo AG, Martín P, et al. Pivotal role for skin transendothelial radio-resistant anti-
1047 inflammatory macrophages in tissue repair. *Elife*. 2016;5.

1048 127. Chen P-Y, Qin L, Baeyens N, Li G, Afolabi T, Budatha M, Tellides G, Schwartz MA, Simons M.
1049 Endothelial-to-mesenchymal transition drives atherosclerosis progression. *J Clin Invest*.
1050 2015;125:4514–28.

1051 128. Manavski Y, Lucas T, Glaser SF, Dorsheimer L, Günther S, Braun T, Rieger MA, Zeiher AM, Boon
1052 RA, Dimmeler S. Clonal Expansion of Endothelial Cells Contributes to Ischemia-Induced
1053 Neovascularization. *Circ Res*. 2018;122:670–677.

1054 129. Iso T, Maeda K, Hanaoka H, Suga T, Goto K, Syamsunarno MRAA, Hishiki T, Nagahata Y, Matsui
1055 H, Arai M, et al. Capillary endothelial fatty acid binding proteins 4 and 5 play a critical role in
1056 fatty acid uptake in heart and skeletal muscle. *Arterioscler Thromb Vasc Biol*. 2013;33:2549–
1057 57.

1058 130. Baer C, Squadrito ML, Iruela-Arispe ML, De Palma M. Reciprocal interactions between
1059 endothelial cells and macrophages in angiogenic vascular niches. *Exp Cell Res*. 2013;319:1626–
1060 34.

1061 131. He H, Xu J, Warren CM, Duan D, Li X, Wu L, Iruela-Arispe ML. Endothelial cells provide an
1062 instructive niche for the differentiation and functional polarization of M2-like macrophages.
1063 *Blood*. 2012;120:3152–62.

1064 132. Maleszewska M, Moonen J-RAJ, Huijkman N, van de Sluis B, Krenning G, Harmsen MC. IL-1β
1065 and TGFβ2 synergistically induce endothelial to mesenchymal transition in an NFκB-
1066 dependent manner. *Immunobiology*. 2013;218:443–54.

1067 133. Russell KS, Yates DP, Kramer CM, Feller A, Mahling P, Colin L, Clough T, Wang T, LaPerna L,
1068 Patel A, et al. A randomized, placebo-controlled trial of canakinumab in patients with
1069 peripheral artery disease. *Vasc Med*. 2019;24:414–421.

1070

1071

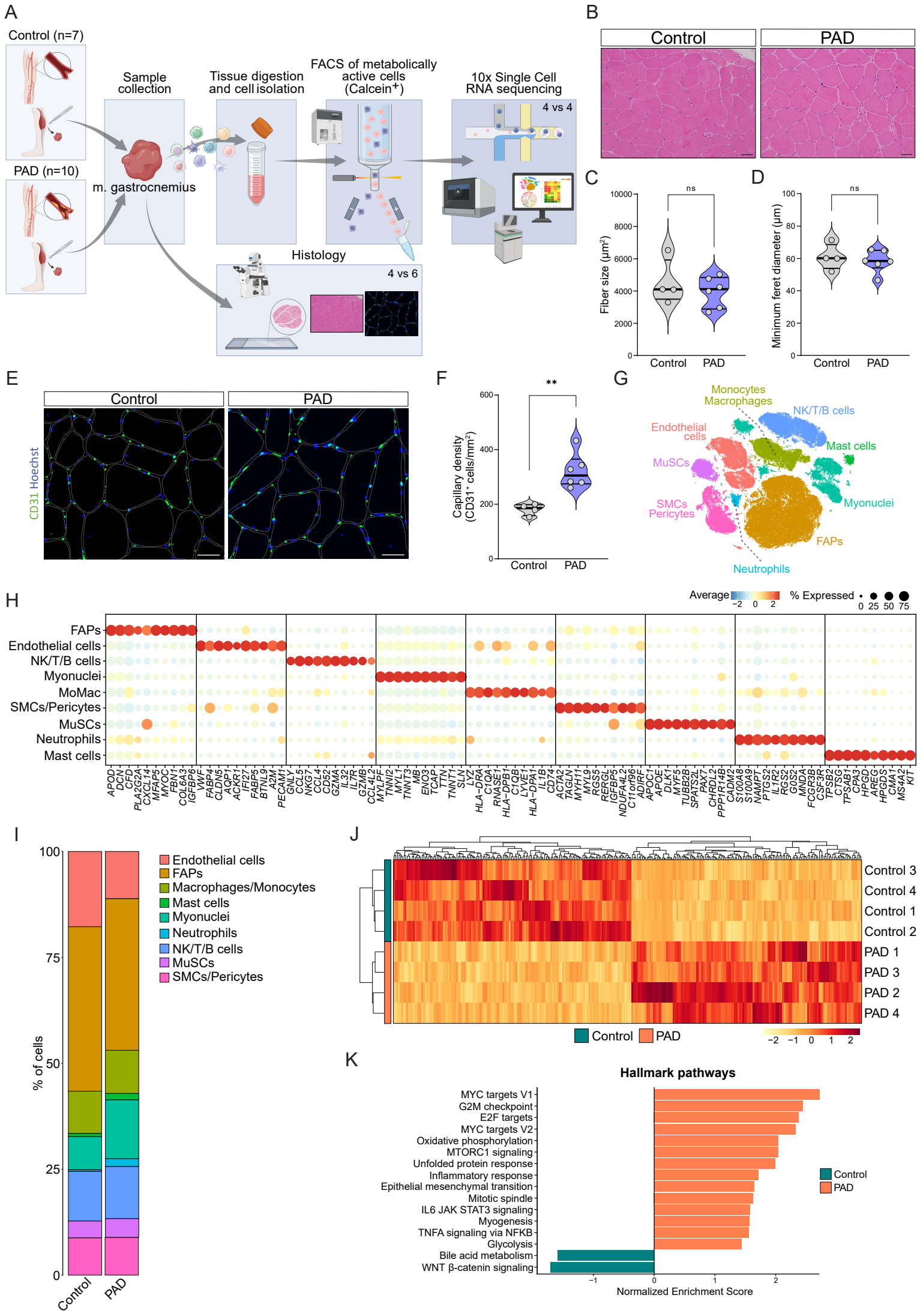
A
Control (n=7)
PAD (n=10)
Sample collection
m. gastrocnemius
Tissue digestion and cell isolation
FACS of metabolically active cells (Calcein+)
10x Single Cell RNA sequencing
4 vs 4
Histology
4 vs 6
B
Control
PAD
C
Fiber size (µm²)
ns
Control
PAD
D
Minimum feret diameter (µm)
ns
Control
PAD
E
Control
PAD
CD31 Hoechst
F
Capillary density (CD31+ cells/mm²)
**
Control
PAD
G
Monocytes Macrophages
NK/T/B cells
Endothelial cells
Mast cells
MuSCs
Myonuclei
SMCs Pericytes
FAPs
Neutrophils
H
Average
% Expressed
FAPs
Endothelial cells
NK/T/B cells
Myonuclei
MoMac
SMCs/Pericytes
MuSCs
Neutrophils
Mast cells
I
% of cells
Control
PAD
Endothelial cells
FAPs
Macrophages/Monocytes
Mast cells
Myonuclei
Neutrophils
NK/T/B cells
MuSCs
SMCs/Pericytes
J
Control 3
Control 4
Control 1
Control 2
PAD 1
PAD 3
PAD 2
PAD 4
Control
PAD
K
Hallmark pathways
MYC targets V1
G2M checkpoint
E2F targets
MYC targets V2
Oxidative phosphorylation
MTORC1 signaling
Unfolded protein response
Inflammatory response
Epithelial mesenchymal transition
Mitotic spindle
IL6 JAK STAT3 signaling
Myogenesis
TNFA signaling via NFKB
Glycolysis
Bile acid metabolism
WNT β-catenin signaling
Control
PAD
Normalized Enrichment Score

1072 **Figure 1. scRNAseq reveals cell heterogeneity in PAD. A**, Graphical abstract of the experimental
1073 approach used in this study. **B**, Representative images of haematoxylin and eosin (H&E)-stained
1074 sections of gastrocnemius muscle from control (n=4) and PAD (n=6) patients (Scale bar: 50 µm). **C,D**,
1075 Quantification of fiber size in μm^2 (**C**) and minimum feret diameter in µm (**D**) from panel B. **E**,
1076 Representative images of gastrocnemius muscle from control (n=4) and PAD (n=6) stained for the EC
1077 marker (CD31, green) and cell nuclei (Hoechst, blue) (Scale bar: 50 µm). Muscle fibers are represented
1078 with white dashed lines. **F**, Quantification of capillary density from panel E measured as the number of
1079 $CD31^+$ cells per mm^2. **G**, TSNE plot of cell populations identified from human gastrocnemius muscle,
1080 color-coded by the identified populations. **H**, Dot plot of centered logcounts values from cell type-
1081 specific marker genes. Color and size of the dots indicate the centered logcount value and the
1082 proportion of cells that express the gene, respectively. **I**, Stacked bar plots showing cluster percentage
1083 in each condition, color-coded by cluster. **J**, Heatmap of centered normalized values from top high
1084 variable genes (adjusted p-value < 0.05) in each patient based on pseudobulk analysis between control
1085 and PAD conditions, color indicates the centered normalized values. **K**, Bar plots showing Normalized
1086 Enrichment Score of significant (adjusted p-value < 0.05) Hallmark pathways (MsigDB) from GSEA
1087 analysis on the pseudobulk dataset, color indicates the condition. Each dot represents a single patient
1088 in panels C,D and F. Student's t test (two-tailed, unpaired, parametric, ns > 0.05, $^{**}p < 0.01$) was used
1089 in C,D and F.

1090

1091

1092

1093

1094

1095

1096

1097

1098

1099

1100

1101

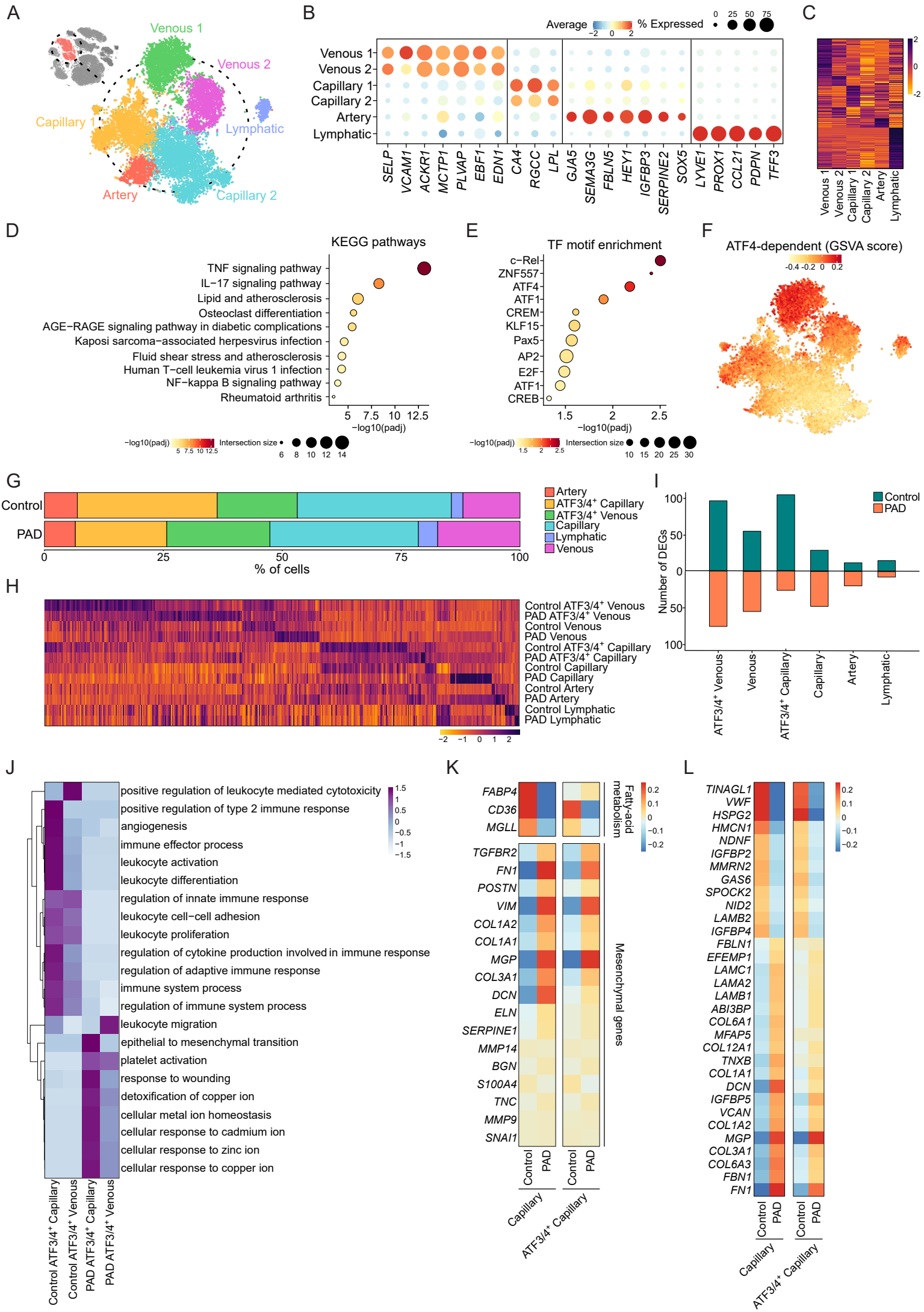
A
Venous 1
Venous 2
Capillary 1
Lymphatic
Artery
Capillary 2
B
Average
% Expressed
Venous 1
Venous 2
Capillary 1
Capillary 2
Artery
Lymphatic
SELP VCAM1 ACKR1 MCTP1 PLVAP EBF1 EDN1 CA4 RGCC LPL GJA5 SEMA3G FBLN5 HEY1 IGFBP3 SERPINE2 SOX5 LYVE1 PROX1 CCL21 PDPN TFF3
C
Venous 1
Venous 2
Capillary 1
Capillary 2
Artery
Lymphatic
D
KEGG pathways
TNF signaling pathway
IL−17 signaling pathway
Lipid and atherosclerosis
Osteoclast differentiation
AGE−RAGE signaling pathway in diabetic complications
Kaposi sarcoma−associated herpesvirus infection
Fluid shear stress and atherosclerosis
Human T−cell leukemia virus 1 infection
NF−kappa B signaling pathway
Rheumatoid arthritis
−log10(padj)
Intersection size
E
TF motif enrichment
c−Rel
ZNF557
ATF4
ATF1
CREM
KLF15
Pax5
AP2
E2F
ATF1
CREB
−log10(padj)
Intersection size
F
ATF4-dependent (GSVA score)
G
Control
PAD
% of cells
Artery
ATF3/4⁺ Capillary
ATF3/4⁺ Venous
Capillary
Lymphatic
Venous
I
Number of DEGs
Control
PAD
ATF3/4⁺ Venous
Venous
ATF3/4⁺ Capillary
Capillary
Artery
Lymphatic
H
Control ATF3/4⁺ Venous
PAD ATF3/4⁺ Venous
Control Venous
PAD Venous
Control ATF3/4⁺ Capillary
PAD ATF3/4⁺ Capillary
Control Capillary
PAD Capillary
Control Artery
PAD Artery
Control Lymphatic
PAD Lymphatic
J
positive regulation of leukocyte mediated cytotoxicity
positive regulation of type 2 immune response
angiogenesis
immune effector process
leukocyte activation
leukocyte differentiation
regulation of innate immune response
leukocyte cell−cell adhesion
leukocyte proliferation
regulation of cytokine production involved in immune response
regulation of adaptive immune response
immune system process
regulation of immune system process
leukocyte migration
epithelial to mesenchymal transition
platelet activation
response to wounding
detoxification of copper ion
cellular metal ion homeostasis
cellular response to cadmium ion
cellular response to zinc ion
cellular response to copper ion
Control ATF3/4⁺ Capillary
Control ATF3/4⁺ Venous
PAD ATF3/4⁺ Capillary
PAD ATF3/4⁺ Venous
K
FABP4
CD36
MGLL
Fatty-acid metabolism
TGFBR2
FN1
POSTN
VIM
COL1A2
COL1A1
MGP
COL3A1
DCN
ELN
SERPINE1
MMP14
BGN
S100A4
TNC
MMP9
SNAI1
Mesenchymal genes
Control
PAD
Capillary
ATF3/4⁺ Capillary
L
TINAGL1
VWF
HSPG2
HMCN1
NDNF
IGFBP2
MMRN2
GAS6
SPOCK2
NID2
LAMB2
IGFBP4
FBLN1
EFEMP1
LAMC1
LAMA2
LAMB1
ABI3BP
COL6A1
MFAP5
COL12A1
TNXB
COL1A1
DCN
IGFBP5
VCAN
COL1A2
MGP
COL3A1
COL6A3
FBN1
FN1
Control
PAD
Capillary
ATF3/4⁺ Capillary

1102 **Figure 2. Human skeletal muscle contains several EC subtypes with different functional properties.**
1103 **A**, TSNE plot of EC subtypes identified from human gastrocnemius muscle, color-coded by the
1104 identified subtypes. **B**, Dot plot of centered logcounts values from EC subtype-specific marker genes.
1105 Color and size of the dots indicate the centered logcount value and the proportion of cells that express
1106 the gene, respectively. **C**, Heatmap of centered logcounts of DEGs (adjusted p-value <0.05) between
1107 EC subtypes, color indicates the centered logcount value. **D**,**E**, ORA analysis from genes upregulated in
1108 Venous 1 compared to Venous 2 (see Figure S1A) using KEGG pathways (**D**) or TF motif enrichment (**E**),
1109 color and size of the dots indicates the -log10 adjusted p-value and the number of genes in each
1110 category (intersection size), respectively. **F**, TSNE plot of GSVA scores using the ATF4 dependent
1111 geneset from Fan et al (see Methods), color-coded by the GSVA score. **G**, Stacked bar plots showing
1112 cluster percentage in each condition, color-coded by cluster. **H**, Heatmap of centered logcounts of
1113 DEGs (adjusted p-value < 0.05) specific for each EC subtype in each condition, color indicates the
1114 centered logcount value. **I**, Bar plots showing the number of DEGs for each EC subtype in each
1115 condition, color indicates the condition. **J**, Heatmap of centered values from ORA analysis over the
1116 DEGs in ATF3/4^{+} venous and capillary ECs between conditions, color indicates the centered values. **K,L**,
1117 Heatmap of centered logcounts values of fatty acid metabolism and mesenchymal markers as defined
1118 in Tombor et al (**K**) and core matrisome genes as defined in Hynes et al (**L**), color indicates the centered
1119 values.

1120

1121

1122

1123

1124

1125

1126

1127

1128

1129

1130

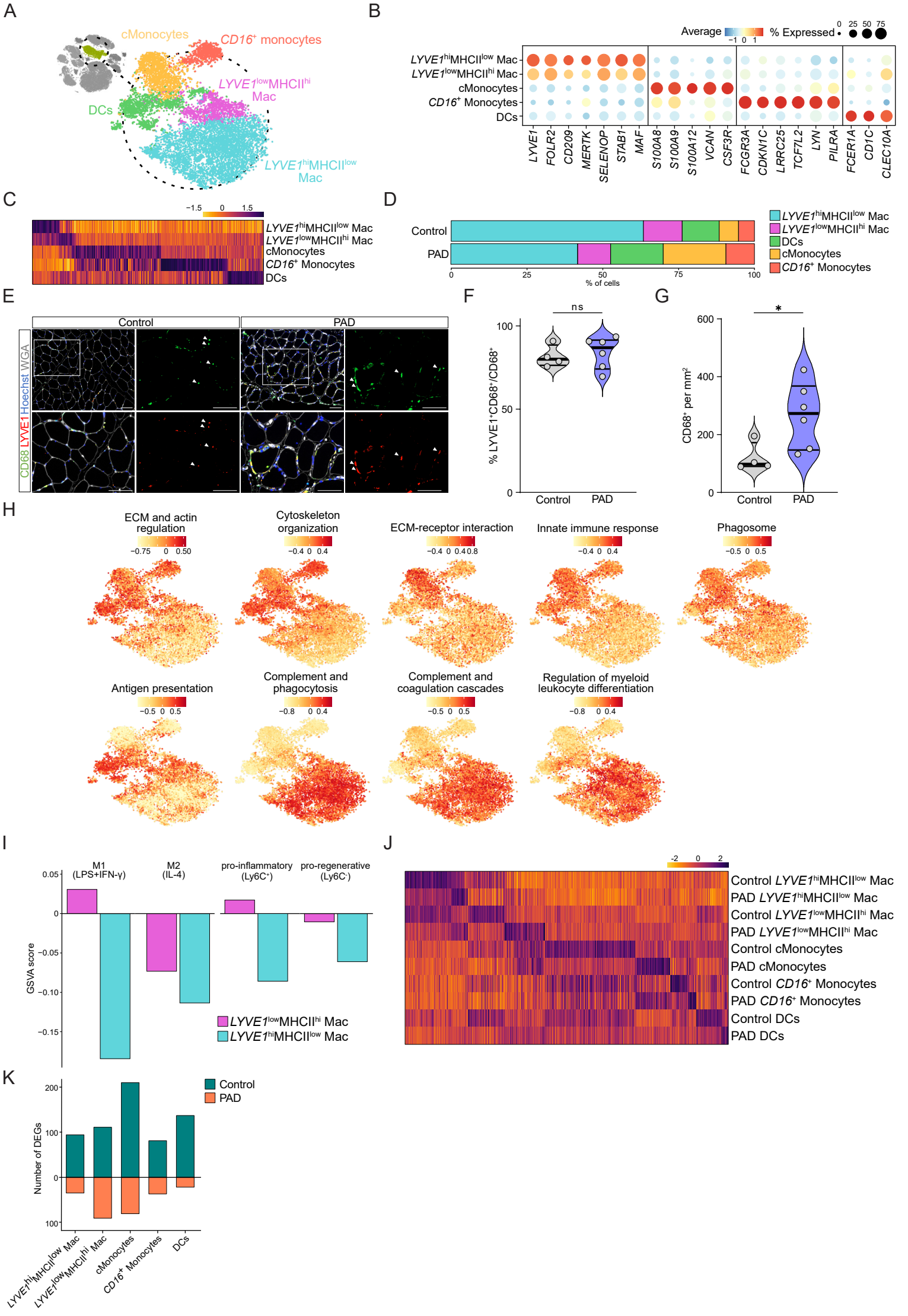
A
cMonocytes
CD16+ monocytes
LYVE1lowMHCIIhi Mac
DCs
LYVE1hiMHCIIlow Mac
B
Average
% Expressed
LYVE1hiMHCIIlow Mac
LYVE1lowMHCIIhi Mac
cMonocytes
CD16+ Monocytes
DCs
LYVE1 FOLR2 CD209 MERTK SELENOP STAB1 MAF S100A8 S100A9 S100A12 VCAN CSF3R FCGR3A CDKN1C LRRC25 TCF7L2 LYN PILRA FCER1A CD1C CLEC10A
C
LYVE1hiMHCIIlow Mac
LYVE1lowMHCIIhi Mac
cMonocytes
CD16+ Monocytes
DCs
D
Control
PAD
% of cells
LYVE1hiMHCIIlow Mac
LYVE1lowMHCIIhi Mac
DCs
cMonocytes
CD16+ Monocytes
E
Control
PAD
CD68 LYVE1 Hoechst WGA
F
ns
% LYVE1+CD68+/CD68+
Control
PAD
G
*
CD68+ per mm2
Control
PAD
H
ECM and actin regulation
Cytoskeleton organization
ECM-receptor interaction
Innate immune response
Phagosome
Antigen presentation
Complement and phagocytosis
Complement and coagulation cascades
Regulation of myeloid leukocyte differentiation
I
M1 (LPS+IFN-γ)
M2 (IL-4)
pro-inflammatory (Ly6C+)
pro-regenerative (Ly6C-)
GSVA score
LYVE1lowMHCIIhi Mac
LYVE1hiMHCIIlow Mac
J
Control LYVE1hiMHCIIlow Mac
PAD LYVE1hiMHCIIlow Mac
Control LYVE1lowMHCIIhi Mac
PAD LYVE1lowMHCIIhi Mac
Control cMonocytes
PAD cMonocytes
Control CD16+ Monocytes
PAD CD16+ Monocytes
Control DCs
PAD DCs
K
Control
PAD
Number of DEGs
LYVE1hiMHCIIlow Mac
LYVE1lowMHCIIhi Mac
cMonocytes
CD16+ Monocytes
DCs

1131 **Figure 3**. **LYVE1^{hi}MHCII^{low} macrophages are the dominant macrophage population in PAD. A**, TSNE
1132 plot of Monocytes/Macrophages subtypes identified from human gastrocnemius muscle, color-coded
1133 by the identified subtypes. **B**, Dot plot of centered logcounts values from MoMac subtype-specific
1134 marker genes. Color and size of the dots indicate the centered logcounts values and the proportion of
1135 cells that express the gene, respectively. **C**, Heatmap of centered logcounts of DEGs (adjusted p-value
1136 <0.05) between MoMac subtypes, color indicates the centered logcount value. **D**, Stacked bar plots
1137 showing cluster percentage in each condition, color-coded by cluster. **E**, Representative images of
1138 gastrocnemius muscle from control (n=4) and PAD (n=6) stained for a pan-macrophage marker (CD68,
1139 green), LYVE1 (red), cell nuclei (Hoechst) and WGA (white) (Scale bar: 50 µm). **F-G**, Quantification of
1140 the percentage of LYVE1^{+}CD68^{+} cells from the total of CD68^{+} cells (**F**) and the total number of
1141 macrophages measured as the number of CD68^{+} cells per mm^{2} (**G**). **H**, TSNE plots showing GSVA scores
1142 for different macrophage activation processes as defined by Sanin et al (see Methods), color-coded by
1143 GSVA score. **I**, GSVA scores from different pro-inflammatory and pro-regenerative signatures as
1144 defined by Varga et al between LYVE1^{hi} and LYVE^{low} macrophages, color-coded by cluster. **J**, Heatmap
1145 of centered logcounts of DEGs (adjusted p-value < 0.05) specific for each MoMac subtype in each
1146 condition, color indicates the centered logcount value. **K**, Bar plot showing the number of DEGs for
1147 each MoMac subtype in each condition, color indicates the condition. Each dot represents a single
1148 patient in panels F and G. Student's t test (two-tailed, unpaired, parametric, ns > 0.05) was used in F
1149 and Mann-Whitney U test (two-tailed, unpaired, non-parametric, $^{*}p < 0.05$). was used in G.

1150

1151

1152

1153

1154

1155

1156

1157

1158

1159

1160

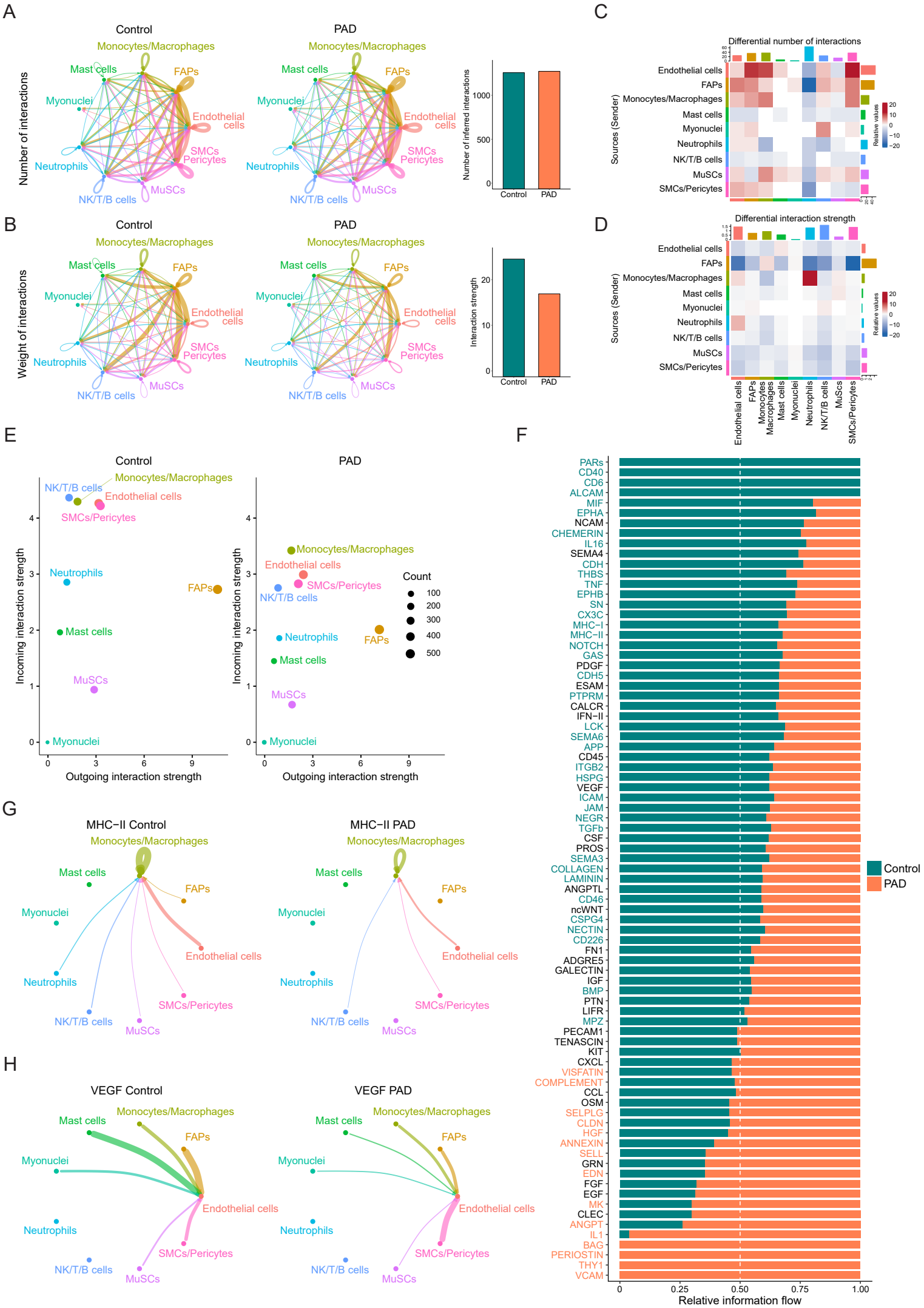
A
Control
PAD
Monocytes/Macrophages
Mast cells
FAPs
Myonuclei
Endothelial cells
SMCs Pericytes
Neutrophils
NK/T/B cells
MuSCs
Number of interactions
Number of inferred interactions
Control
PAD
B
Weight of interactions
Interaction strength
C
Differential number of interactions
Sources (Sender)
Relative values
D
Differential interaction strength
Endothelial cells
FAPs
Monocytes/Macrophages
Mast cells
Myonuclei
Neutrophils
NK/T/B cells
MuSCs
SMCs/Pericytes
E
Control
PAD
Incoming interaction strength
Outgoing interaction strength
Count
100
200
300
400
500
F
PARs
CD40
CD6
ALCAM
MIF
EPHA
NCAM
CHEMERIN
IL16
SEMA4
CDH
THBS
TNF
EPHB
SN
CX3C
MHC−I
MHC−II
NOTCH
GAS
PDGF
CDH5
ESAM
PTPRM
CALCR
IFN−II
LCK
SEMA6
APP
CD45
ITGB2
HSPG
VEGF
ICAM
JAM
NEGR
TGFb
CSF
PROS
SEMA3
COLLAGEN
LAMININ
ANGPTL
CD46
ncWNT
CSPG4
NECTIN
CD226
FN1
ADGRE5
GALECTIN
IGF
BMP
PTN
LIFR
MPZ
PECAM1
TENASCIN
KIT
CXCL
VISFATIN
COMPLEMENT
CCL
OSM
SELPLG
CLDN
HGF
ANNEXIN
SELL
GRN
EDN
FGF
EGF
MK
CLEC
ANGPT
IL1
BAG
PERIOSTIN
THY1
VCAM
Control
PAD
Relative information flow
G
MHC−II Control
MHC−II PAD
H
VEGF Control
VEGF PAD

1161 **Figure 4. Cellular communication in human skeletal muscle is profoundly altered in PAD. A-B**, Circle
1162 plots showing the number (**A**) and weight (**B**) of inferred interactions between cell types in control and
1163 PAD (left and middle plots) and bar plots quantifying these parameters (right plots). Color and width
1164 of the edges indicates the sender and number or weight of interactions, respectively. **C-D**, Heatmaps
1165 showing increased (red) or decreased (blue) number (**C**) and weight (**D**) of inferred interactions in PAD.
1166 Labels in the left side indicates the cell type expressing the ligands and bottom labels the cell types
1167 receiving them. **E**, Scatter plots showing the strength of the outgoing (x-axis) and incoming (y-axis)
1168 interactions for each cell type in control (left) and PAD (right). Color and size of the dots indicate the
1169 cell type and the number of inferred interactions, respectively. **F**, Bar plots showing the relative
1170 information flow for significant communication pathways between control and PAD. **G-H**, Circle plots
1171 showing MHC-II (**G**) and VEGF (**H**) communication in control (left) and PAD (right). Color and width of
1172 the edges indicates the sender and weight of interactions, respectively.

1173

1174

1175

1176

1177

1178

1179

1180

1181

1182

1183

1184

1185

1186

1187

1188

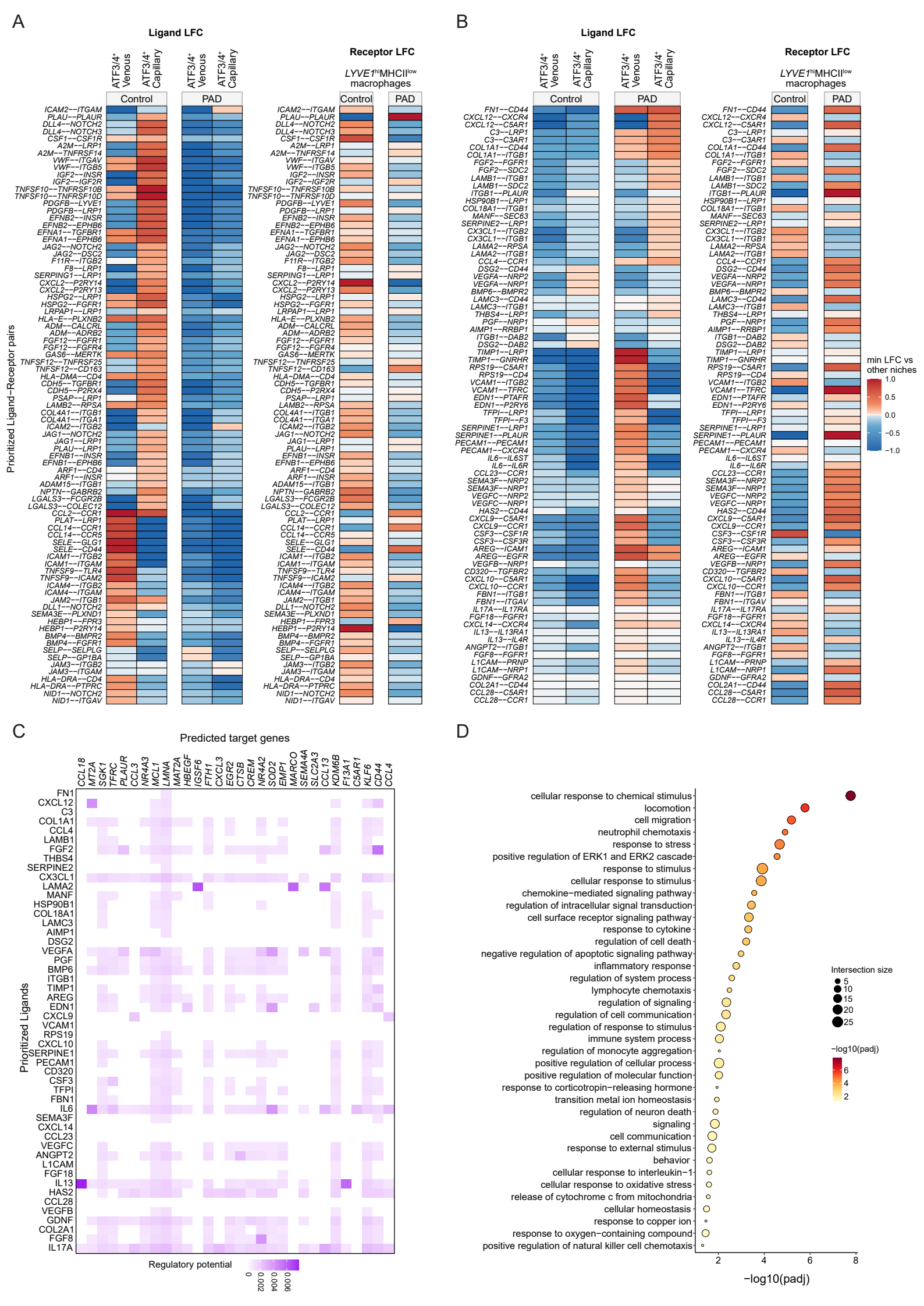
A
Ligand LFC
Receptor LFC
ATF3/4+ Venous
ATF3/4+ Capillary
LYVE1hiMHCIIlow macrophages
Control
PAD
Prioritized Ligand−Receptor pairs
min LFC vs other niches
B
C
Predicted target genes
Prioritized Ligands
Regulatory potential
D
cellular response to chemical stimulus
locomotion
cell migration
neutrophil chemotaxis
response to stress
positive regulation of ERK1 and ERK2 cascade
response to stimulus
cellular response to stimulus
chemokine−mediated signaling pathway
regulation of intracellular signal transduction
cell surface receptor signaling pathway
response to cytokine
regulation of cell death
negative regulation of apoptotic signaling pathway
inflammatory response
regulation of system process
lymphocyte chemotaxis
regulation of signaling
regulation of cell communication
regulation of response to stimulus
immune system process
regulation of monocyte aggregation
positive regulation of cellular process
positive regulation of molecular function
response to corticotropin−releasing hormone
transition metal ion homeostasis
regulation of neuron death
signaling
cell communication
response to external stimulus
behavior
cellular response to interleukin−1
cellular response to oxidative stress
release of cytochrome c from mitochondria
cellular homeostasis
response to copper ion
response to oxygen−containing compound
positive regulation of natural killer cell chemotaxis
Intersection size
−log10(padj)

1189 **Figure 5. Cellular communication between ATF3/4^{+} ECs and LYVE1^{hi}MHCII^{low} macrophages is altered**
1190 **during PAD. A-B**, Heatmaps showing downregulated (**A**) and upregulated (**B**) ligand-receptor (LR) pairs
1191 in PAD. In each panel, left part indicates the ligand log fold change (LFC) in ATF3/4^{+} ECs and right part
1192 the receptor LFC in LYVE1^{hi}MHCII^{low} macrophages from each LR pair. Color indicates the LFC. **C**,
1193 Heatmap showing the regulatory potential of ATF3/4^{+} ECs ligands upregulated in PAD (left labels) over
1194 the downstream target genes upregulated in LYVE1^{hi}MHCII^{low} macrophages (top labels). Color indicates
1195 the regulatory potential. **D**, Dot plot showing ORA results from the predicted targets in panel C. Color
1196 and size of the dots indicate -log10 adjusted p-value and number of genes in each category
1197 (intersection size), respectively.

1198

1199

1200

1201

1202

1203

1204

1205

1206

1207

1208

1209

1210

1211

1212

1213

1214

1215

1216 # TABLES

	Control	PAD
Number of subjects	7	10
Average age (years)	71.6±2.6	74.1±2.7
Ankle Brachial Index	1.16±0.08	0.78±0.13*
Fontaine classification I/IIa/IIb/III/IV	7/0/0/0/0	0/0/6/2/2
scRNAseq/Histology	4/4[†]	4/6
Gender (male/female)	7/0	10/0
Smoking (never/current/former)	2/1/4	3/5/2
Obesity (BMI > 30 kg/m^2)	1	0
Diabetes Mellitus	2	3
Hypertension	7	8
Hyperlipidemia	7	8
Statins	7	7
Anti-platelet agents	7	8
Antihypertensive drugs	7	7
Antidiabetic agents	2	3
Involved side (left/right)	3/4	5/5

1217 *Table 1.Patient demographics. Continuous values are presented as mean ± standard error of the mean. BMI indicates Body*
1218 *Mass Index. *p < 0.05, Student's t test (unpaired, two-tailed). † Sample from one subject was used for both scRNAseq and*
1219 *histology.*